Aerodynamic Testing of the Orion Launch Abort Tower Separation with Jettison Motor Jet Interactions

Matthew N. Rhode* and David T. Chan.†
NASA Langley Research Center, Hampton, VA 23681

Charles J. Niskey‡
Black Ram Engineering Services LLC, Hampton, VA 23681

Thomas M. Wilson§
ESCG/ERC Inc, Houston, TX 77058

The aerodynamic database for the Orion Launch Abort System (LAS) was developed largely from wind tunnel tests involving powered jet simulations of the rocket exhaust plumes, supported by computational fluid dynamics (CFD) simulations. The LAS contains three solid rocket motors used in various phases of an abort to provide propulsion, steering, and Launch Abort Tower (LAT) jettison from the Crew Module (CM). This paper describes a pair of wind tunnel experiments performed at transonic and supersonic speeds to determine the aerodynamic effects due to proximity and jet interactions during LAT jettison from the CM at the end of an abort. The tests were run using two different scale models at angles of attack from 150° to 200°, sideslip angles from -10° to +10°, and a range of powered thrust levels from the jettison motors to match various jet simulation parameters with flight values. Separation movements between the CM and LAT included axial and vertical translations as well as relative pitch angle between the two bodies. The paper details aspects of the model design, nozzle scaling methodology, instrumentation, testing procedures, and data reduction. Sample data are shown to highlight trends seen in the results.

Nomenclature

Symbols

A	=	nozzle cross-sectional area, in^2
C_F	=	thrust coefficient
D	=	model reference diameter, in
F	=	nozzle thrust, lbf
M	=	Mach number
p	=	pressure, psf, psia
q	=	dynamic pressure, psf
Re	=	Reynolds number
S	=	model reference area, in^2
T	=	temperature, °F, °R
V	=	velocity, ft/sec
w	=	mass flow rate, lbm/sec
X,Y,Z	=	Cartesian coordinate axes, in
α	=	angle of attack, deg
β	=	angle of sideslip, deg

* Research Aerospace Engineer, Aerothermodynamics Branch, Mail Stop 408A, Senior Member, AIAA.
† Research Aerospace Engineer, Configuration Aerodynamics Branch, Mail Stop 499, Member, AIAA.
‡ Aerospace Engineer, Senior Member, AIAA.
§ Aerospace Engineer, Aerothermal & Flight Mechanics, 2222 Bay Area Blvd, Member, AIAA.

γ = specific heat ratio
$\Delta\alpha$ = relative pitch angle between CM and LAT, deg
ΔX = axial separation distance between CM and LAT, in
ΔY = lateral separation distance between CM and LAT, in
ΔZ = vertical separation distance between CM and LAT, in
ρ = density, slug/ft^3
ϕ = roll angle, deg

Subscripts

F = flight condition
J = nozzle exit
T = total or stagnation
WT = wind tunnel condition
∞ = freestream
$*$ = nozzle throat

Acronyms

ACM	Attitude Control Motor
AEDC	Arnold Engineering Development Center
ALAS	Alternate Launch Abort System
AM	Abort Motor
API	Application Programming Interface
ARC	Ames Research Center
BOS	Background-Oriented Schlieren
BPC	Boost Protective Cover
CEV	Crew Exploration Vehicle
CFD	Computational Fluid Dynamics
CLV	Crew Launch Vehicle
CM	Crew Module
DTC	Digital Temperature Compensation
ESP	Electronically-Scanned Pressure
ISS	International Space Station
JI	Jet Interaction
JM	Jettison Motor
LaRC	Langley Research Center
LAS	Launch Abort System
LAT	Launch Abort Tower
LAV	Launch Abort Vehicle
LEO	Low-Earth Orbit
MRC	Moment Reference Center
OML	Outer Mold Line
PWT	Propulsion Wind Tunnel
RCS	Reaction Control System
RTD	Resistance Temperature Detector
UPWT	Unitary Plan Wind Tunnel
USAF	United States Air Force

I. Introduction

THE Orion Crew Exploration Vehicle (CEV) is presently being developed under NASA's Constellation program to provide human access to low-earth orbit (LEO) and the International Space Station (ISS) as well as missions to the Moon and other parts of the solar system.[1] The CEV is designed to launch atop the Ares I Crew Launch Vehicle (CLV), a two-stage booster employing both solid and liquid-fueled rocket motors and leveraging heavily

upon existing hardware and infrastructure from the Space Shuttle program. For crew safety, the CEV will utilize a Launch Abort System (LAS) that is capable of pulling the Crew Module (CM) capsule away from the CLV in the event of an emergency on the launch pad or at any point along the ascent trajectory. The LAS, shown in Figure 1, consists of a Launch Abort Tower (LAT) containing an ogive-conical fairing that surrounds the CM along with a cylindrical tower containing three solid rocket motors used during an abort. The abort motor (AM) is a high-thrust, high-impulse engine used to pull the CM quickly away from the CLV. The engine is a reverse-flow design where the propellant sits below the nozzles and occupies the lower half of the tower. The hot combustion gases turn through an angle less than 180 degrees to exit out four nozzles that utilize varying throat diameters to align the thrust vector with the vehicle center of gravity. The attitude control motor (ACM) occupies the top portion of the tower and consists of a single solid rocket motor connected to eight axisymmetric nozzles arranged circumferentially around the tower and perpendicular to the centerline axis of the vehicle. The ACM is used to provide steering and control of the vehicle during an abort via actuator-controlled pintles within each nozzle throat to vary the effective throat area and thus the thrust. The jettison motor (JM) lies approximately in the middle of the tower and is used to pull the LAT away from the CM in the final stages of an abort or during a normal launch at a point in the ascent trajectory where the LAT is no longer required and is jettisoned to eliminate extraneous weight. The JM employs four nozzles that are scarfed flush with the surface of the tower. One of the four nozzles has a smaller throat to provide a thrust offset necessary to move the LAT away from the CLV flight path during ascent. The combination of the LAT mated to the CM is referred to as the Launch Abort Vehicle (LAV).

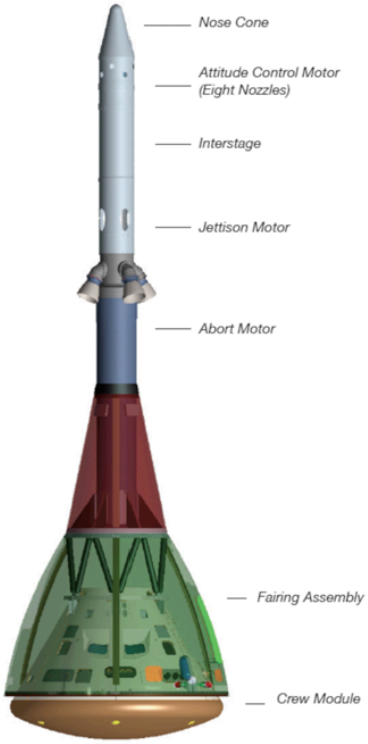

Figure 1. Orion Launch Abort System (LAS).

A typical abort sequence is shown in Figure 2. In the event of an emergency, the AM fires to pull the LAV away from the CLV while the ACM fires to provide steering and control. After the AM burns out, the vehicle continues to coast, with the ACM providing trim near zero angle of attack. The ACM then turns the LAV to a heat-shield-forward orientation, damping out pitch rates prior to tower jettison. Pyrotechnic bolts discharge to separate the LAT from the CM, while the JM fires nearly simultaneously to slow the LAT and allow the CM to fall clear prior to parachute deployment. The entire abort sequence takes approximately 20-30 seconds to complete.

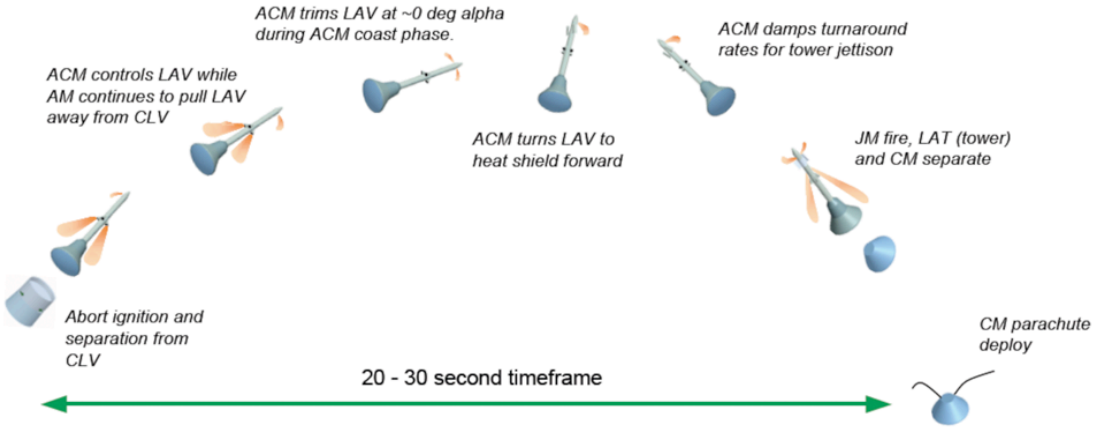

Figure 2. Typical Launch Abort Sequence.

The aerodynamic complexities that exist in all phases of the abort, such as plume jet interaction (JI) and two-body proximity effects, necessitated the use of wind tunnel testing for aerodynamic database development and calibration of computational fluid dynamics (CFD) codes. Two such tests were a pair of LAT-CM separation tests with JM jet interactions at transonic and supersonic Mach numbers and designated CEV Test 24-AA and 25-AA, respectively. The tests were performed at the USAF Arnold Engineering Development Center (AEDC) Propulsion Wind Tunnel (PWT) 16T in May-Jun 2009[2], and at the NASA Ames Research Center (ARC) 9x7-Foot Supersonic Wind Tunnel in Jan-Feb 2010, covering a combined Mach number range from 0.3 to 2.5. This paper describes the wind tunnel tests and discusses aspects of the experiment design and model design as well as the nozzle scaling required for matching pertinent jet simulation parameters. Important features of the data reduction and post-test processing are presented, along with a selection of results to highlight data quality and general trends. Due to export control restrictions, certain information has been omitted from the body of the paper as well as plots and figures.

II. Experiment Design

A. Separation Analysis

Upon initiation of the LAT jettison during the final stages of an abort, the LAT and CM are subject to translational and rotational movements relative to each other. CEV Tests 24-AA and 25-AA were conducted to ensure that no large separation and/or jet interaction effects exist that could result in contact between the two bodies during the time that they are in close proximity to one another. Monte Carlo simulations of the abort, performed using the then-current aerodynamic database, trajectory, and vehicle mass properties data, were used to determine the range of separation movements required in the wind tunnel tests. The use of body symmetry allowed a reduction in movements to two translations, ΔX and ΔZ, and one rotation, $\Delta\alpha$, which greatly simplified the model design and sizably reduced the test matrix requirements. Figure 3 shows the coordinate system and definitions for the separation movements, which are defined relative to the LAT reference frame. Note that due to the definitions, the axial separation distance is a negative value. The tests were performed using normalized separation distances of $\Delta X/D$ = -1.00 to 0 and $\Delta Z/D$ = -0.20 to +0.20, and a relative pitch angle, $\Delta\alpha$, from 0 to 6°.

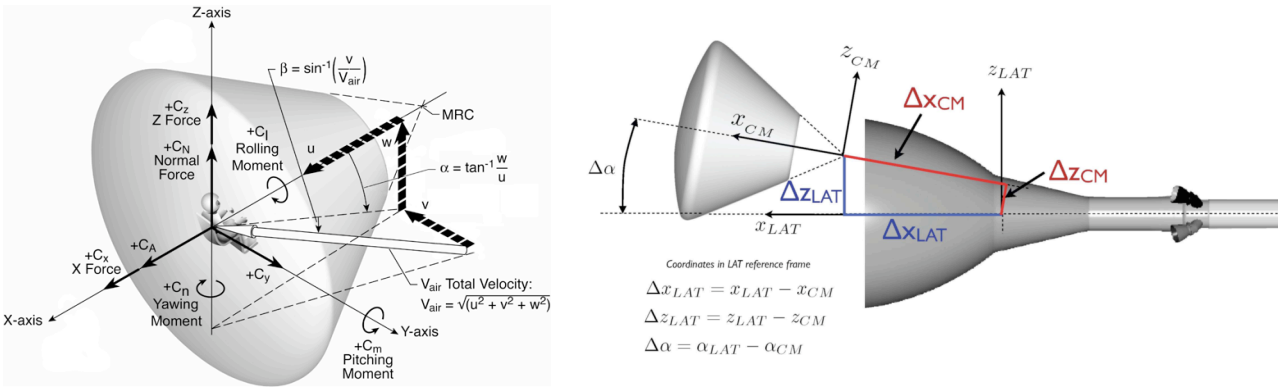

(a) Coordinate System (b) Separation Movements

Figure 3. Coordinate System and Separation Movement Definitions.

B. Nozzle Scaling Methodology

For proper simulation of aerodynamic jet interactions, it is necessary to match jet thrust and momentum relative to their respective freestream quantities, as well as matching the plume shape.[3] It is not sufficient merely to scale the nozzles geometrically, particularly for cold-flow simulations in wind tunnel facilities. Tests 24-AA and 25-AA utilized similar but slightly different nozzle scaling methodologies to determine the nozzle geometries for the respective wind tunnel models. For Test 24-AA, the nozzle geometry was chosen to allow the simultaneous matching of momentum ratio, thrust coefficient, and jet-to-freestream static pressure ratio across the range of

freestream Mach numbers. For Test 25-AA, the nozzle scaling parameters were modified to allow better matching of the plume shapes at the higher jet-to-freestream static pressure ratios associated with supersonic freestream conditions.

The parameter, momentum ratio, is defined as

$$\frac{(wV)_J}{(wV)_\infty} = \frac{\rho_J V_J^2 A_J}{\rho_\infty V_\infty^2 S} = \left(\frac{p_J}{p_\infty}\right)\left(\frac{\gamma_J M_J^2}{\gamma_\infty M_\infty^2}\right)\left(\frac{A_J}{S}\right) \tag{1}$$

It can be seen through inspection that if we match the freestream Mach number between flight and wind tunnel conditions, geometrically scale the nozzle exit area, and match the jet-to-freestream static pressure ratio, p_J/p_∞, then the momentum ratio is matched if

$$\left[\gamma_J M_J^2\right]_{WT} = \left[\gamma_J M_J^2\right]_F \tag{2}$$

For cold-flow simulations with high pressure air, the nozzle exit ratio of specific heats, γ_J, is almost always greater than the flight value, thus necessitating a lower nozzle exit Mach number in the wind tunnel model to match momentum ratio. In the Orion program, the matching parameter of interest for aerodynamic jet interactions was the thrust coefficient**, defined as

$$C_F \equiv \frac{F_J}{q_\infty S} = 2\left(\frac{p_J}{p_\infty}\right)\left(\frac{\gamma_J M_J^2 + 1}{\gamma_\infty M_\infty^2}\right)\left(\frac{A_J}{S}\right) \tag{3}$$

Thrust coefficient is simultaneously matched given the assumptions above and setting the nozzle exit Mach number per Equation 2, as was done for Test 24-AA.

In Test 25-AA, the nozzle geometry was determined by equating

$$\left[\frac{\gamma_J M_J^2}{\beta_J}\right]_{WT} = \left[\frac{\gamma_J M_J^2}{\beta_J}\right]_F ; \text{ where } \beta_J = \sqrt{M_J^2 - 1} \tag{4}$$

Using the parameter in Equation 4, the momentum ratio and thrust coefficient can be written, respectively, as

$$\frac{(wV)_J}{(wV)_\infty} = \beta_J\left(\frac{p_J}{p_\infty}\right)\left(\frac{\gamma_J M_J^2/\beta_J}{\gamma_\infty M_\infty^2}\right)\left(\frac{A_J}{S}\right) \tag{5}$$

and

$$C_F = 2\left(\frac{p_J}{p_\infty}\right)\left(\frac{\beta_J\left(\gamma_J M_J^2/\beta_J\right) + 1}{\gamma_\infty M_\infty^2}\right)\left(\frac{A_J}{S}\right) \tag{6}$$

According to Reference 3, nozzle scaling by way of Equation 4 is intended to allow the local plume expansion angle at the nozzle exit to be matched exactly. However, this matching is strictly valid only for low values of jet-to-freestream static pressure ratio, as might be encountered at low subsonic conditions or for motors operating at low combustion chamber pressures. For the present scaling analysis, the specification of the nozzle exit Mach number via Equation 4 permits the wind tunnel model nozzles to operate at slightly higher static pressure ratios than the flight nozzles when the thrust coefficient (Equation 6) is matched, as shown below in Equation 7. Note that since $\gamma_{J_F} < \gamma_{J_{WT}}$, Equation 4 dictates that $M_{J_F} > M_{J_{WT}}$, and thus $\beta_{J_F} > \beta_{J_{WT}}$.

$$\left(\frac{p_J}{p_\infty}\right)_{WT} \approx \frac{\beta_{J_F}}{\beta_{J_{WT}}}\left(\frac{p_J}{p_\infty}\right)_F \tag{7}$$

** Vacuum thrust was used in the nozzle scaling for the JM, since the ambient pressure term in the net thrust cancels out due to nozzle exit area symmetry in the four JM nozzles.

The plume shape tends to be a strong function of the static pressure ratio, p_J/p_∞, and a somewhat lesser function of the ratio of specific heats, γ_J. Because of the lower γ_J, the flight nozzle plume expands to a larger diameter than the wind tunnel model nozzle plume for a given static pressure ratio and nozzle exit Mach number. Thus, specifying the model nozzle geometry by way of Equation 4 allows the nozzle to operate at a higher static pressure ratio when matching thrust coefficient, and therefore provides a better match to the fight plume shape, as will be shown below.

The methodology above was used to size the three larger-throat-diameter JM nozzles for the wind tunnel model. The fourth smaller-throat nozzle was sized to match the thrust coefficient of its corresponding flight nozzle while operating at the same model plenum conditions as the other three nozzles. This also preserved the offset angle of the total thrust vector from the centerline axis.

The nozzle exit conditions and gas properties for the flight nozzles were computed via the NASA Glenn Chemical Equilibrium with Applications (CEA) code, using the area ratio, combustion chamber conditions, and propellant mole fractions as inputs. In the analysis, the nozzle was treated as an axisymmetric nozzle, a valid assumption provided that the Mach angle is less than the scarf angle of the nozzle.[4] Because one of the four JM nozzles has a smaller throat and thus higher nozzle exit Mach number, the analysis was performed for both the "large" and "small" JM nozzles.

C. Nozzle Plume Shape Analysis

Static plume shapes were computed for both the flight and wind tunnel conditions using the PLUME code[5], an axisymmetric Euler code for computing both the plume boundary and the surrounding lip shock. Here, the plume boundary is defined as the locus of points where the plume static pressure equals the surrounding ambient pressure. Inputs to the PLUME code include the nozzle exit Mach number, jet and freestream specific heat ratios, and the nozzle exit-to-freestream ratios of pressure, temperature, and molecular weight. Based on early PLUME code predictions, the nozzle exit angle was adjusted to provide a better match to the initial plume expansion angle and the overall plume shape in general. A comparison of the wind tunnel and flight plumes for the larger-throat JM nozzle at a jet-to-freestream static pressure ratio equivalent to a Mach 1.6 flight condition is shown in Figure 4. With thrust coefficient matched to the flight value, the modified nozzle scaling used for Test 25-AA shows an improvement in matching the flight plume shape as compared to that for Test 24-AA. Over the Mach number ranges of the respective wind tunnel tests, the maximum plume diameter was within 10% of the flight value for Test 24-AA and within 5% for Test 25-AA.

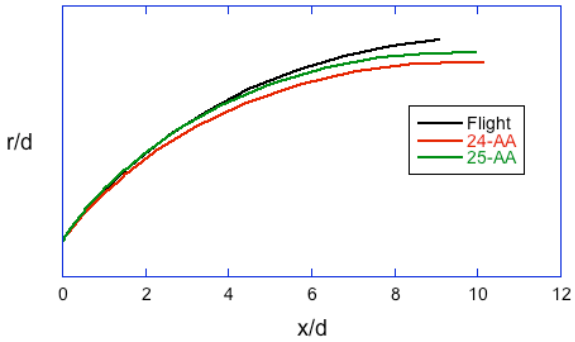

Figure 4. Comparison of Plume Shapes for a Matched C_T at Mach 1.6.

D. Test Conditions

The matching of the nozzle scaling parameters was dependent on both the tunnel operating conditions and the model plenum conditions, as expressed through the nozzle static pressure ratio as

$$\frac{p_J}{p_\infty} = \frac{p_{T_J}\left(p_J/p_{T_J}\right)}{p_{T_\infty}\left(p_\infty/p_{T_\infty}\right)} = \frac{p_{T_J}}{p_{T_\infty}}\frac{f\left(M_J\right)}{f\left(M_\infty\right)} \tag{8}$$

Thus, given a freestream Mach number and a nozzle static pressure ratio, either matched to its corresponding flight value (Test 24-AA) or determined via Equation 7 (Test 25-AA), the facility total pressure and model plenum pressure can be selected. The facility operating pressure is often selected as a compromise between a good Reynolds number simulation and a value that keeps the model plenum pressures required for jet simulation within reasonable limits. For CEV Tests 24-AA and 25-AA, the operating conditions were chosen to provide constant unit Reynolds numbers of $1.0\text{x}10^6$/ft and $1.5\text{x}10^6$/ft, respectively. The freestream Mach numbers for the two tests were selected to match the cardinal Mach numbers in the aerodynamic database.[6] A spreadsheet program was then written to calculate the model plenum pressures required for matching momentum ratio and thrust coefficient to flight. The

model plenum temperature was selected to avoid air liquefaction at the nozzle exit, based on the theoretical air saturation curve.[7] The nominal facility operating conditions are listed in Table 1 along with estimated uncertainties for both the measured and calculated flowfield parameters.

Table 1. Facility Operating Conditions and Uncertainties for CEV Tests 24-AA and 25-AA.

Test	M_∞	p_T, psf	T_T, R	p_∞, psf	q_∞, psf	Re, 1/ft
24-AA	0.3 ± 0.002	1139.9 ± 0.40	560 ± 3	1070.9 ± 0.80	67.5 ± 0.86	1.0e+06
	0.5 ± 0.003	732.8 ± 0.40	560 ± 3	617.8 ± 0.93	108.1 ± 0.89	1.0e+06
	0.7 ± 0.003	578.2 ± 0.40	560 ± 3	416.8 ± 0.99	143.0 ± 0.81	1.0e+06
	0.9 ± 0.003	509.8 ± 0.40	560 ± 3	301.4 ± 1.00	170.9 ± 0.66	1.0e+06
	1.1 ± 0.004	482.9 ± 0.40	560 ± 3	226.2 ± 0.95	191.6 ± 0.44	1.0e+06
	1.2 ± 0.004	479.4 ± 0.40	560 ± 3	197.7 ± 0.91	199.3 ± 0.33	1.0e+06
25-AA	1.6 ± 0.003	763.6 ± 0.65	560 ± 4	179.7 ± 0.81	321.9 ± 0.35	1.5e+06
	1.8 ± 0.003	816.2 ± 0.65	560 ± 4	142.1 ± 0.66	322.2 ± 0.48	1.5e+06
	2.0 ± 0.003	885.8 ± 0.65	560 ± 4	113.2 ± 0.53	864.7 ± 0.58	1.5e+06
	2.2 ± 0.003	971.2 ± 0.65	560 ± 4	90.8 ± 0.43	307.7 ± 0.64	1.5e+06
	2.5 ± 0.003	1128.0 ± 0.65	560 ± 4	66.0 ± 0.31	288.8 ± 0.68	1.5e+06

III. Facility Description

A. AEDC Propulsion Wind Tunnel (PWT) 16T

AEDC PWT 16T is a closed circuit, continuous-flow, variable-density transonic wind tunnel that operates at Mach numbers from 0.06 to 1.60 and stagnation pressures from 200 to 3950 psf, using air as the test medium. Over the operating envelope, unit Reynolds number ranges from approximately 0.2×10^6 to 7.4×10^6 per foot. The facility is driven by a 271,000-hp drive system turning a three-stage, axial-flow compressor. At Mach numbers greater than 0.6, the compressor turns at a constant 600 rpm, using variable inlet guide vanes and stators to satisfy volume flow requirements. Sub-synchronous, variable-speed operation of the compressor is used at lower subsonic Mach numbers.[8]

The test section measures 16×16 feet in cross-section by 40 feet in length and is enclosed by 60-degree inclined-hole perforated walls of 6% fixed porosity. The top and bottom walls are fixed while the sidewall angle can be varied from 1.5 degrees convergence to 1-degree divergence to minimize axial Mach number gradients and buoyancy effects. The entire test section and supporting structure is constructed as a separate unit, known as a test cart, and is removable from the tunnel circuit. Model installation and checkout are performed at the Model Installation Building (MIB), and the test cart is moved on rails to the facility prior to the start of the test. Several test carts are available for use, depending on the test requirements. The CEV Test 24-AA utilized Cart 1, with the High-Angle Automated Sting (HAAS) support system providing pitch angles from -3.6° to +43° at pitch rates up to 4 deg/sec. Roll angles of ±180° are possible using the primary roll mechanism, with roll rates from 2-20 deg/sec. The data acquisition and signal conditioning systems are located onboard the test cart to reduce signal attenuation via shorter cable leads, and to increase test productivity by using the same instrumentation systems for buildup and test, eliminating the need to recalibrate or re-zero instrumentation at the facility.

Several small optical ports are located in the test section walls for use with cameras, lamps, and lasers for a variety of optical measurement techniques such as pressure and temperature-sensitive paints, non-intrusive laser diagnostics, and background-oriented schlieren.

A high-pressure air supply system is available to support cold-flow or hot-flow jet simulations at flow rates of up to 60 lbm/sec at pressures up to 3000 psia at the tunnel shell. A steam heat exchanger is used to regulate airflow temperatures up to 200 °F. A series of critical-flow venturis are available for installation in the auxiliary air supply path for accurate measurement of the mass flow rate. The entire system is computer controlled to precisely regulate air pressure, temperature, and mass flow rate in a test article.

B. NASA Ames 9x7-Foot Supersonic Wind Tunnel

The NASA Ames 9x7-Foot Supersonic Wind Tunnel is a closed circuit, continuous-flow, variable-density supersonic facility equipped with an asymmetric sliding-block nozzle that provides continuous Mach number adjustment from 1.54 to 2.56. Stagnation pressure can be varied from 634 to 4250 psf, with a maximum stagnation temperature of 600 °R. Over the operating envelope of the facility, the unit Reynolds number ranges from 0.9×10^6 to 5.8×10^6 per foot. Tunnel flow is produced using an 11-stage, axial-flow compressor powered by four variable-speed induction motors.[9]

The test section measures 9×7 feet in cross section and 18 feet in length with hatches in the ceiling and side of the tunnel for model access and installation. A traversing, horizontal strut spans the test section and contains the model support system that uses a knuckle-sleeve mechanism to position the test article at attitudes up to those circumscribed by a 15-degree half-angle cone. Bent adapters are available to alter the range of model angles. Typically, a model is pitched through angle of attack in the horizontal plane of the tunnel so that the traverse capability of the strut can be used to maintain the center of rotation near the tunnel centerline.

Two 28-inch-diameter windows at two different axial stations in each sidewall provide optical access for schlieren and other flow visualization techniques. Each window is mounted offset in a 50-inch-diameter disk that can be manually rotated to vary the window position relative to the model and test section.

High-pressure air for jet simulations is supplied by dual, independently controlled auxiliary air systems at flow rates up to a total of 80 lbm/sec at pressures up to 3000 psia. Air from one of these systems can be heated to temperatures of 200 °F using a 1-MW heater. Flow rates are measured using sub-critical-flow venturi meters, while pressures and flow rates are regulated with a multi-poppet digital control valve.

IV. Model Description

A. 7%-Scale Test 24-AA Model

CEV Test 24-AA was performed at AEDC PWT 16T using a 7%-scale model of the ALAS 606E configuration. The model scale was chosen to allow sufficient volume for instrumentation, hardware, and the routing of instrumentation leads and tubing below the outer mold line (OML), while at the same time being small enough to limit blockage effects and keep the mass flow requirements within facility limits for constant operations. OML features larger than 0.5 inches full scale were represented in the model and include details such as the windows, hatches, and reaction control system (RCS) nozzles on the CM backshell; the umbilical cutout and dummy AM nozzles on the LAT; and the attachment truss structure, crew access platform[††], and recessed surfaces inside the Boost Protective Cover (BPC) cavity on the LAT. An illustration of the model is shown in Figure 5, and a diagram of the model installation in the test section of AEDC 16T is given in Figure 6. Photographs of two different model configurations are shown in Figure 7. Of note are the asymmetric features on the inside of the BPC cavity such as the surface recessions and the crew platform present only on the port side of the model, as detailed in Figure 7(b).

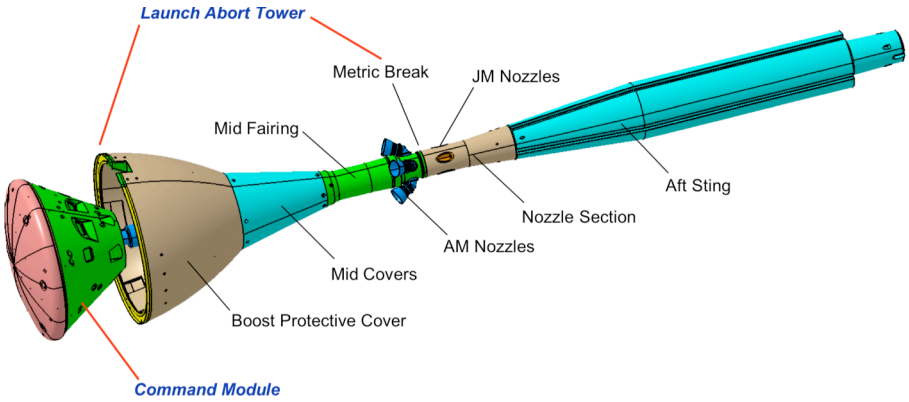

Figure 5. 7%-Scale Test 24-AA Model, Shown at ΔX/D = -0.50.

[††] The crew access platform is a perforated walkway between the CM and BPC that allows the crew to enter and exit the CM through a hatch in the BPC while at the launch facility.

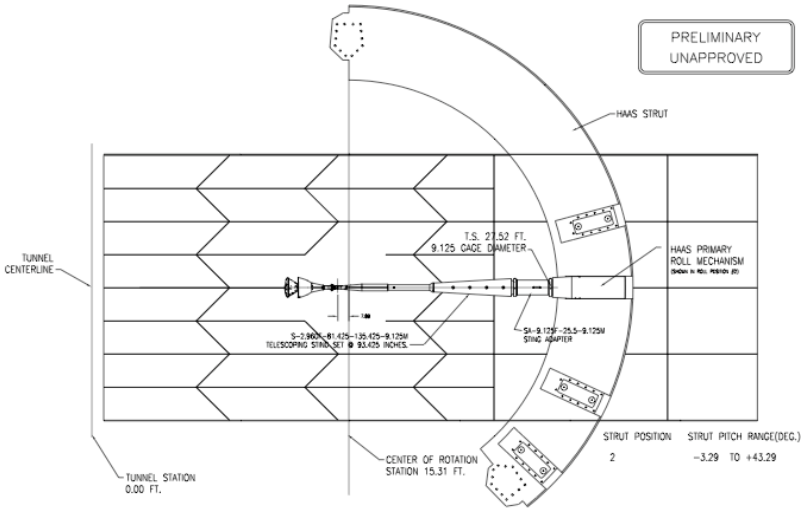

Figure 6. Model Installation Diagram for Test 24-AA.

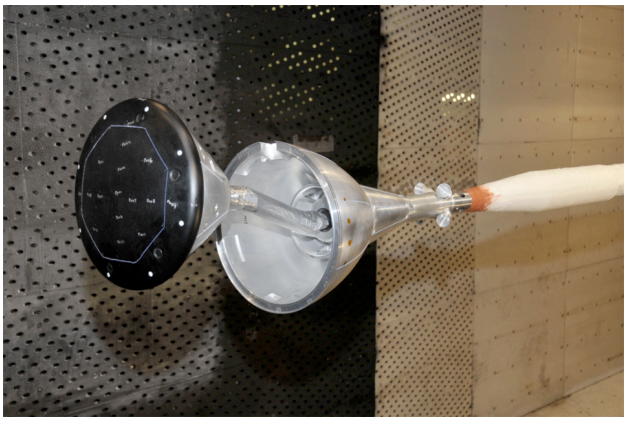

(a) CM + LAT Configuration:
$\Delta X/D = -1.00$, $\Delta Z/D = -0.20$, $\Delta\alpha = 6°$

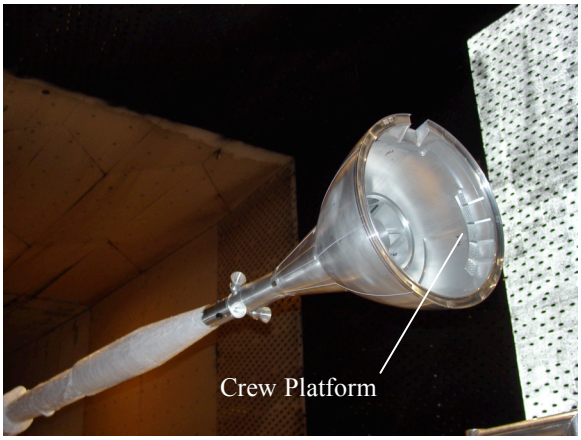

(b) LAT-Only Configuration

Figure 7. Test 24-AA Model at AEDC 16T

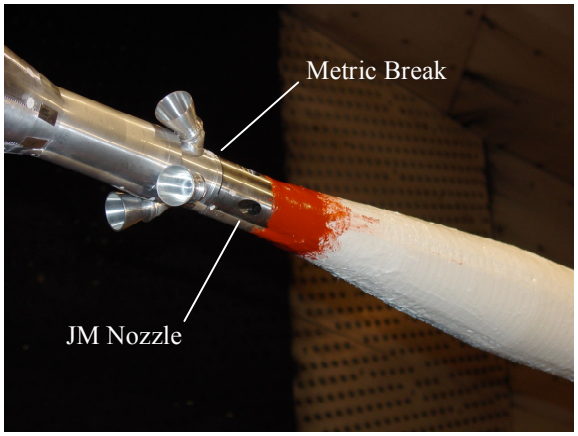

Figure 8. Jettison Motor Nozzles for Test 24-AA Model

The limited model volume in the LAT portion of the model, along with the requirement for LAT axial force measurements, led to the design of a partially-metric model with a metric break just downstream, relative to the freestream flow, of the AM nozzles, as shown in Figure 8. The powered JM nozzles were thus non-metric, which obviated the need for thrust tares during the test. The loss of aerodynamic contribution from the upper portion of the LAT was deemed minimal, as the focus of the test was on the coupled proximity/JI effects that occur upstream, and at a distance, from the metric break.

A brush seal was initially installed inside of the metric break to minimize mass flow in and out of the gap. The brush seal was ultimately removed during model buildup due to problems with fouling and because of interference with the routing of instrumentation leads.

Separation movements between the CM and LAT were attained using either a straight sting or a manually articulated sting between the two bodies. The straight sting was used for small axial separation distances with no ΔZ or $\Delta\alpha$ movements. Several dowel holes were located in the sting to set the separation distance. As illustrated in Figure 9, the articulated sting consisted of a translating Fwd Adapter attached to the LAT, a Balance Adapter connected directly to the CM force balance, and an interposing link containing 3-degree gear teeth on the end radii. Two interchangeable links of differing lengths were used to achieve the combinations of separation movements. Geared keys were used at each end of the link to set the position and lock the assembly together. A photograph of the articulated sting is shown in Figure 10. The Fwd Adapter part included multiple dowel holes to maintain constant ΔX separation distances as the articulated sting was foreshortened during ΔZ movements. The hardware allowed combinations of separation movements of $\Delta X/D$ = -1.00 to 0, $\Delta Z/D$ = -0.20 to +0.20, and $\Delta\alpha$ = 0 to 6°. Additionally, the model could be run in the CM-only and LAT-only configurations, which served as the baseline configurations (infinite separation distances) for determining the combined proximity/JI increments. A description of the various model configurations that were tested is given in Table 2.

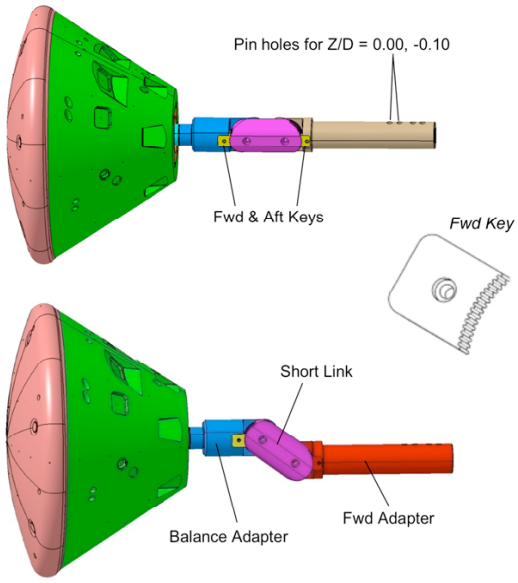

Figure 9. Illustration of Articulated Sting for Test 24-AA Model.

Careful attention was paid to the design of the model plenum to avoid sharp edges and rapid shape transitions that can result in head pressure losses. The plenum was a continuation of the straight airflow path from the facility support sting, with a conical flow diverter located just before the entrances to the nozzles. The nozzle parts were fabricated as separate inserts that were press-fit into place and retained with a permanent dowel pin. The throats were designed to have a short straight section and shallow approach and exit angles to eliminate potential flow separation. The efficiency of the nozzle and plenum design is reflected in the measured discharge coefficients that ranged from $0.96 \le C_d \le 0.99 \pm 0.005$.

Figure 10. Photograph of Test 24-AA Articulated Sting with Short and Long Links.

Instrumentation in the model included six-component force balances and pressure transducers in both the CM and LAT, along with pressure and temperature measurements in the model plenum. Details of the instrumentation are discussed in Section V. In the design of the model, particular attention was given to the routing of instrumentation leads and pneumatic lines to keep them below the OML surface to avoid interfering with the external flow around the model, and to avoid damage to the leads themselves from the air flow. The cables and

tubing were modeled into the CAD file, and slots, passages, and relief areas were designed and machined into the model structure to provide paths for these instrumentation lines. Even with these designed passages, the clearances for the various cables and tubing were small, as shown at the metric break in Figure 11, and instances of model fouling and residual loads due to bridging the balance with the instrumentation leads were encountered during the initial model buildup. Several routing options were tried during model buildup, and extra material was machined away from the inside of one model part to provide additional clearance around the leads. Ultimately, the problems were corrected, and subsequent balance check loadings revealed no fouling or significant balance strains due to the cables and pressure tubing.

Table 2. Description of Tested Model Configurations.

ID #	Description	ΔX/D	ΔZ/D	Δα, deg	Test 24-AA	Test 25-AA
101	CM	∞	0	0	x	x
102	LAT	∞	0	0	x	x
103	CM + LAT	-0.02	0	0	x	x
104	CM + LAT	-0.05	0	0	x	x
105	CM + LAT	-0.10	0	0	x	x
106	CM + LAT	-0.25	0	0	x	x
107	CM + LAT	-0.50	0	0	x	x
108	CM + LAT	-0.50	0	3	x	x
109	CM + LAT	-0.50	-0.10	3	x	x
110	CM + LAT	-0.50	-0.10	0	x	x
111	CM + LAT	-1.00	0	0	x	x
112	CM + LAT	-1.00	0	6	x	x
113	CM + LAT	-1.00	-0.20	6	x	x
114	CM + LAT	-1.00	-0.20	0	x	x
115	LAV	0	0	0	x	x
116	CM + LAT	-0.50	0.10	0		x
117	CM + LAT	-1.00	0.20	0		x
118	CM + LAT	-1.00	0	3		x
119	CM + LAT	-1.00	-0.20	3		x

B. 3%-Scale Test 25-AA Model

The CEV Test 25-AA model was a 3%-scale hybrid of the ALAS 606E configuration for the LAT and the 606G configuration for the CM. The change in the model CM configuration from 606E to 606G was made partway through the model design process to accommodate an adjustment to the vehicle backshell angle designed to increase volume for packaging of the parachute systems.

The test was originally slated for both 4x4-foot test sections of the NASA Langley Research Center (LaRC) Unitary Plan Wind Tunnel (UPWT), covering a Mach number range from 1.5 to 4.6. The model scale was selected with the aid of CFD computations using the OVERFLOW code to check for blockage, interference, or shock reflections that could adversely affect the data or prevent operation of the facility altogether. CFD predictions were made at facility freestream conditions for a range of model configurations, angles of attack, thrust coefficients, and both with and without test section walls to generate comparisons of wind tunnel versus free air conditions. Results from the OVERFLOW code showed significant blockage effects at Mach 1.6 at scales as small as 2%. For this reason, the lower Mach number portion of the test was shifted to the larger ARC 9x7-Foot SWT. An example case run for the ARC 9x7-Foot SWT at Mach 1.6 and at angle of attack is shown in Figure 12. The model scale was selected for blockage-free testing in the high Mach number test section ($2.5 \le M_\infty \le 4.6$) of NASA LaRC UPWT, and the OML retained the same detail features as for the 24-AA model. Likewise, the model was partially metric, with the metric break in the same location as its larger counterpart. An illustration of the overall model and a test section installation diagram are shown in Figure 13 and Figure 14, respectively, while a photograph of the model is shown in Figure 15.

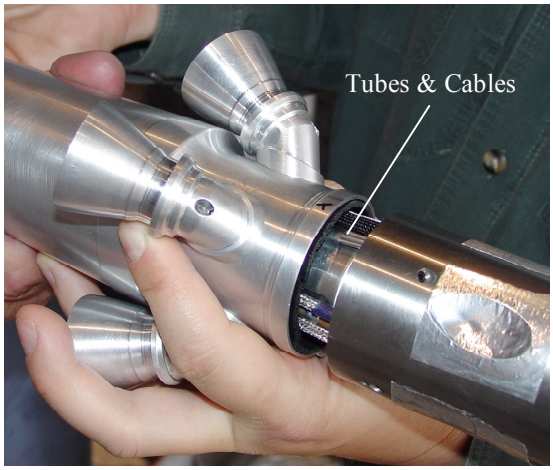

Figure 11. Routing of Instrumentation Lines Across Metric Break for Test 24-AA Model.

Because of the smaller scale of the model, an articulated sting between the CM and LAT was not practical, so individual stings were fabricated to allow the same combination of separation movements as for Test 24-AA. A total of 13 separation stings were built, including an extra-long version for the CM-only configuration to minimize

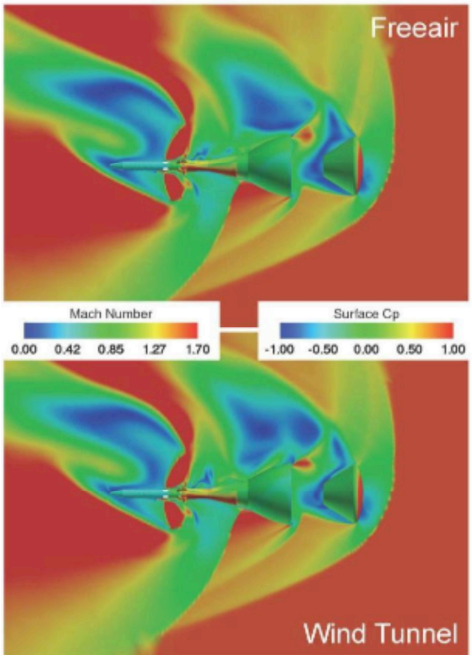

Figure 12. OVERFLOW CFD Computations at Mach 1.6 for NASA ARC 9x7-Foot SWT.

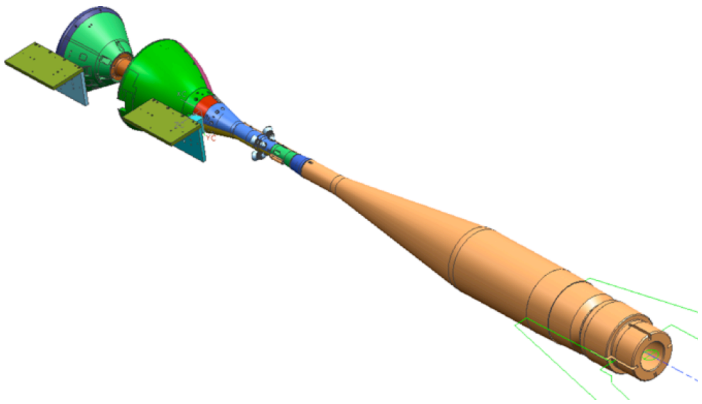

Figure 13. 3%-Scale Test 25-AA Model, Shown with Level Plates.

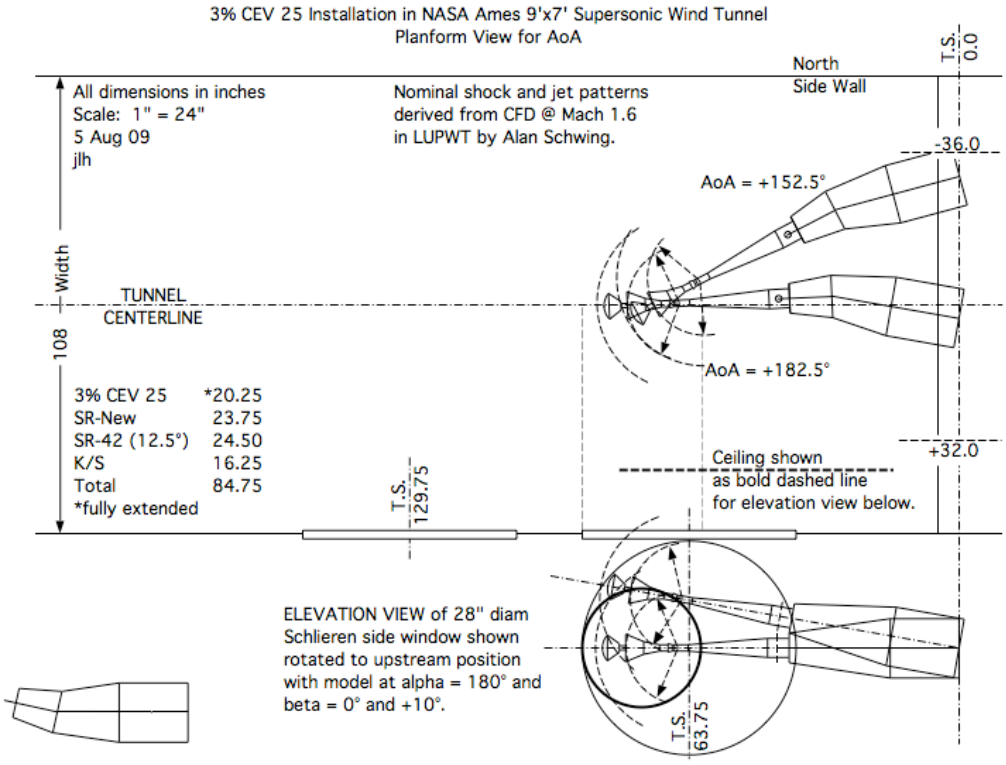

Figure 14. Model Installation Diagram for Test 25-AA.

interference effects on the base from a downstream diameter increase. Each sting contained a circular flange at each end that connected to mating flanges on parts of the CM and LAT. A slot was machined along the length of each sting, including the flanges, to accommodate the CM balance cable and allow separation sting changes without having to disconnect the balance cable or pressure tubing at either end. Keys were fitted to the mating flanges to take the roll torque in shear. An exploded view illustration of the model showing the separation sting concept is shown in Figure 16.

Figure 15. Test 25-AA Model in NASA Ames 9x7-Foot SWT.

Six-component force balances were used in both the CM and LAT portions of the model. The smaller size of the model did not allow for surface pressure measurements via pressure instrumentation located inside the model. Limited base and sting-cavity pressure measurements were made on the CM using pressure tubing routed through the model to instrumentation located within the facility support strut. Similar pressure measurements were made within the metric break.

The balance cables for both the CM and LAT balances, along with tubing for plenum and model surface pressure measurements, were routed around the model plenum by utilizing the space under the raceways, as shown in Figure 17. The height of the raceways on the wind tunnel model was artificially increased over that of the flight vehicle geometry to obtain the volume necessary for routing of the instrumentation leads and tubing, with the raceways included on both sides of the metric break. Also shown in Figure 17 is the rake for measuring total pressure within the model plenum.

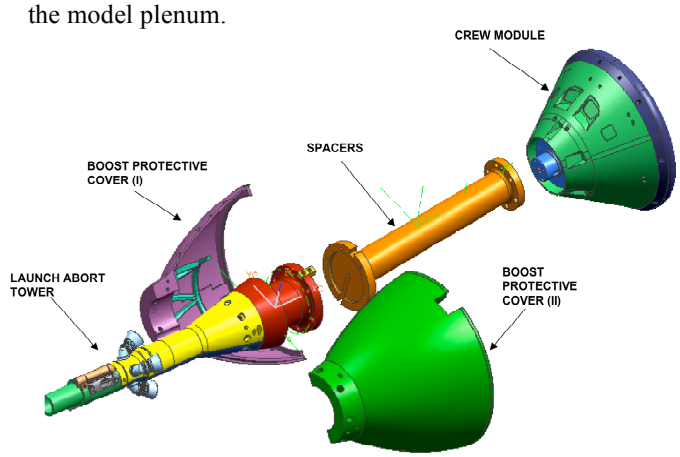

Figure 16. Exploded View of Test 25-AA Model Showing Separation Sting.

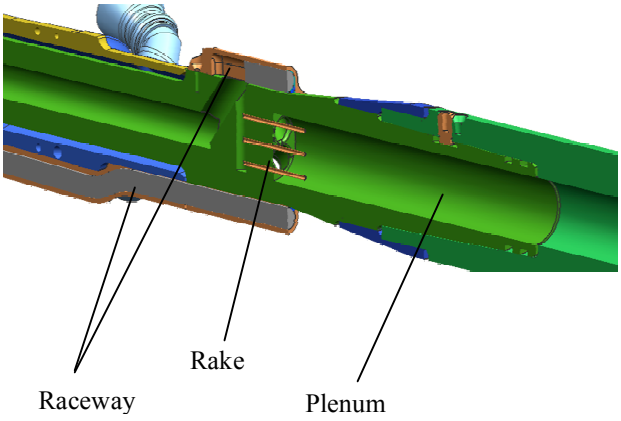

Figure 17. Balance Cable Routing for Test 25-AA Model.

V. Instrumentation

A. CEV Test 24-AA

The primary instruments for Test 24-AA were force and moment balances located in the CM and LAT portions of the model. The CM utilized the NASA LaRC 2043 six-component, direct-read balance while the LAT was instrumented with the NASA ARC Mk XXVIA six-component TASK balance. Both balances were refurbished, re-gauged, and recalibrated prior to the test. The calibrated load ranges for the balances, along with calibration uncertainties, are given in Table 3. Note that while the CM balance measured just the loads on the CM, the LAT balance measured the combined CM+LAT loads. The resultant load center was generally well forward of the LAT balance gauge sections, particularly at the larger separation distances, which resulted in increased balance

measurement uncertainties due to the larger balance component interactions and non-linearities associated with the high pitching moment loads.

Table 3. Balance Calibration Load Ranges and Uncertainties for CEV Tests 24-AA and 25-AA.

Test	Balance	AF, lbf	SF, lbf	NF, lbf	RM, in-lbf	PM, in-lbf	YM, in-lbf
24-AA	2043	450 ± 0.27	100 ± 0.15	250 ± 0.60	150 ± 0.48	1000 ± 0.60	500 ± 0.45
	MK XXVIA	2000 ± 5.42	1600 ± 1.02	2000 ± 2.98	700 ± 2.30	3350 ± 2.71	2120 ± 3.01
25-AA	MK IVA	250 ± 0.10	250 ± 0.66	250 ± 0.74	250 ± 0.50	250 ± 0.34	210 ± 0.27
	MK VII	500 ± 0.23	600 ± 0.80	1000 ± 0.62	150 ± 0.52	1300 ± 0.88	600 ± 0.99

Modifications were made to both balance cables to better suit the test requirements. The CM balance cable was shortened to lessen the volume of cable required for stowage inside of the LAT, as some amount of cable slack was necessary to accommodate the range of separation movements. The wiring of the LAT balance would normally place the voltage sensing at the connector on the end of the cable. Because the cable was routed past the hot model plenum, there was concern that temperature increases in the cable wiring could cause localized changes in electrical resistance and thus create unmeasured drifts in the balance gage voltage. Accordingly, the cable was rewired to place the voltage sensing just behind the balance taper and away from the model plenum.

Each balance contained instrumentation for measuring temperatures within the structure of the balance. The CM balance used three resistance-temperature detectors (RTD) arrayed down the length of the balance, with the wiring included in the balance cable and multi-pin connector. The LAT balance included four Type J thermocouples ($32 \leq T \leq 1382 \pm 5$ °F), with leads external to the balance cable. Unfortunately, by the time the test began, only one of these thermocouples was working. To compensate, bare-bead thermocouples were spot-welded to the external surface of the balance adapter to give some idea of the longitudinal temperature gradients along the balance.

The CM and LAT each contained a 64-port, 15 ± 0.005-psid, digital-temperature-compensation (DTC) ESP module for surface pressure measurements. A total of 61 pressures were measured on the CM via 0.040-inch-diameter pressure tubing: 21 ports on the heat shield, 24 ports on the backshell OML, 1 port in the center of the each of the 4 windows, 8 base pressure ports, and 4 sting-cavity ports, as illustrated in Figure 18. For the LAT, a total of 16 pressures were measured: 8 ports inside the BPC cavity, 4 ports on the BPC OML, and 4 ports within the metric break.

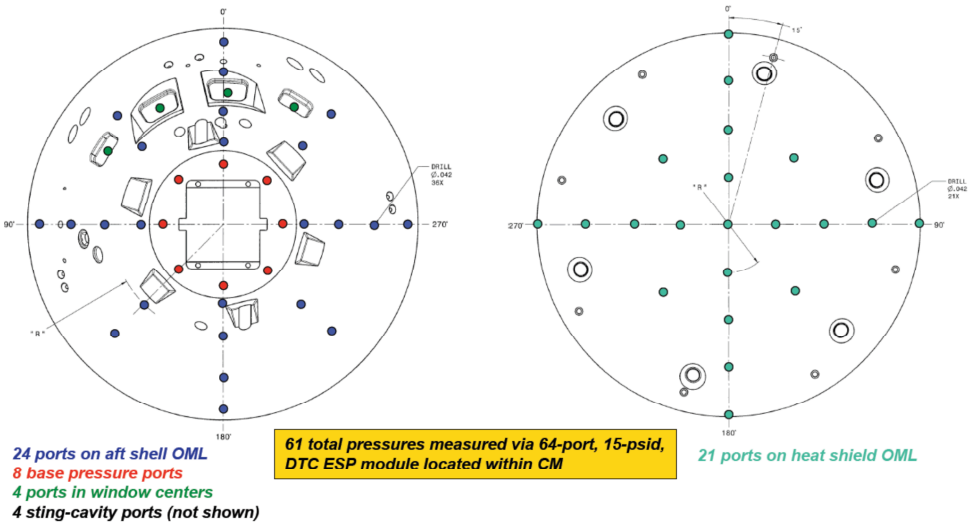

Figure 18. Crew Module Pressure Port Locations for Test 24-AA Model.

Angles of attack and sideslip were determined from the measured model support system pitch and roll angles, deflections calculated using measured balance loads and calibrated sting-balance deflection constants, and balance-to-model angular offsets verified during model buildup. Uncertainty in angle of attack and sideslip for the LAT part of the model was estimated to be ±0.04° and ±0.11°, respectively. A single, pitch-axis Q-Flex accelerometer was located inside of the CM and used to verify the model angles for wind-off conditions. Wind-on accelerometer readings were not used due to vibrations that degraded the quality of the measurements.

Plenum pressure was measured via a 3-probe total pressure rake mounted inside the model plenum and connected to individual 2000 ± 0.5-psia Mensor pressure transducers located outside of the model. An additional plenum static pressure was used to obtain the plenum Mach number via the total-to-static pressure ratio. The measured plenum Mach number was determined to be within 0.02 of its pre-test estimated value. Plenum temperature was quantified using three miniature Type K shielded thermocouple probes (-328 ≤ T ≤ 2282 ± 5 °F).

Mass flow was measured using a calibrated, 0.6479-inch-diameter critical-flow venturi meter supplied by the facility.[10] The venturi inlet pressure was measured using two 3000 ± 0.75-psia Mensor pressure transducers, while temperature was determined using a pair of shielded thermocouple probes with accuracies of ±3 °R. Weight flow measurement uncertainty was estimated to be approximately ±0.05 lbm/sec.

B. CEV Test 25-AA

Similar to its transonic counterpart, the primary instruments in Test 25-AA were a pair of force and moment balances located in the CM and LAT. The NASA ARC Mk IVA six-component TASK balance was used in the CM, while the LAT used a six-component TASK balance supplied by Triumph Force Measurement Systems and designated as the Mk VII balance. Both balances were recalibrated prior to the test. The calibrated load ranges and uncertainties for the balances are given in Table 3.

The smaller model volume precluded the measurement of surface pressures via ESP modules located within the model. Four base pressures and a single sting-cavity pressure were measured on the CM using a 15 ± 0.005-psid, DTC ESP module located within an instrumentation housing on the model support strut. The base pressure ports were located on the aft-facing flange surface of each separation sting, and routed to the ESP module by a combination of stainless steel and flexible pressure tubing. Pressures were also measured in the metric break using the ESP module.

Angles of attack and sideslip were determined from encoders within the model support strut knuckle-sleeve mechanism, deflections calculated using measured balance loads and calibrated sting-balance deflection constants, and balance-to-model angular offsets verified during model buildup. Uncertainty in angle of attack and sideslip for the LAT part of the model was estimated to be ±0.05°.

The model plenum pressure was determined using three total pressures and a single static pressure connected to individual 2500 ± 2.5-psia Kulite pressure transducers. Two shielded Type K thermocouple probes (-328 ≤ T ≤ 2282 ± 5 °F) were used to measure the plenum temperature.

Mass flow was measured using a calibrated, facility-supplied Flow Systems subcritical-flow venturi meter with a 1.970-inch-diameter throat. The venturi inlet pressure was measured using a 3000 ± 0.9-psia Paroscientific pressure transducer while the pressure difference between the inlet and throat was determined via a 26 ± 0.013-psid Rosemount differential pressure transducer. Flow temperature was obtained from a platinum RTD probe located downstream of the venturi throat, with an accuracy of ±1 °R. Over the range of flow rates seen during the test, the weight flow measurement uncertainty was approximately ±0.07 lbm/sec.

VI. Testing and Data Reduction

During the model buildup prior to each test, extensive loadings were performed to verify balance accuracy and to ascertain the sting-balance deflection constants for each model configuration. A photograph of the check loading hardware and setup for Test 24-AA is shown in Figure 19 and a sample result is shown in Figure 20. The check loading process uncovered instances of fouling onto the non-metric portion of the model that required modifications to the model and the routing of instrumentation leads. This was especially an issue for Test 24-AA, given the increased instrumentation requirements associated with internally-mounted ESP modules and the minimal volume provided for routing cables and tubing beneath the OML.

Boundary layer transition strips consisting of cylindrical tape dots were applied in an octagonal array on the heat shield surface of the CM as well as in longitudinal strips along the CM backshell and outer surface of the LAT every

45° around the model. The tape dots were 0.0114 inches in height and 0.05 inches in diameter, with a spacing of 0.100 inches on centers. The trip height and location on the heat shield were determined from boundary layer properties acquired from CFD solutions runs at facility freestream conditions, along with well-established trip sizing guidelines.[11] The longitudinal trip arrays were included in an effort to trip crossflow at higher angles of attack. The transition strips can be seen in the photograph of the Test 24-AA model in Figure 7.

In both tests, the start of any block of data runs was preceded by a period of test operations in which high-pressure air was blown through the model to preheat the model and piping system in order to stabilize temperatures. For Test 24-AA, the model was pitched continuously through an angle of attack range from 150° to 200° at a pitch rate of 1 deg/sec while acquiring data at a sampling rate of 100 samples/sec using a 1-Hz low-pass filter. The use of continuous-pitch test operations resulted in a considerable time savings as well as an increase in data density that revealed features in the results that may have been missed with pitch-pause data acquisition. Moreover, model and balance dynamics were found to be reduced in comparison to the standard pitch-pause method. In Test 25-AA, the model was pitched continuously at 1.5 deg/sec through an angle of attack from 152.2° to 182.5° at $\beta=0°$, with less angle of attack range at non-zero sideslip angles due to the mechanical limitations of the knuckle-sleeve mechanism on the model support strut. Early in each test, runs were made pitching the model from low to high, and then high to low angle of attack to check for flow hysteresis.

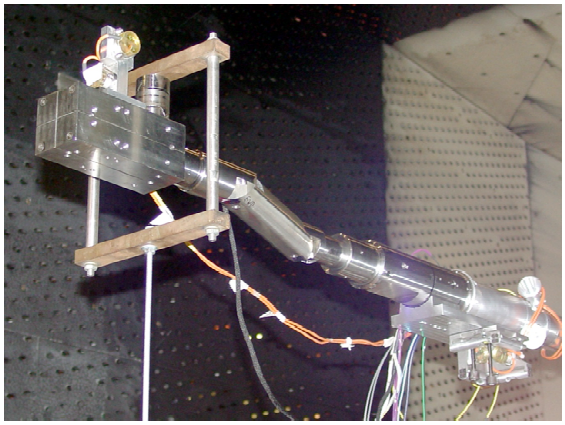

Figure 19. Balance Check Loading Apparatus, Test 24-AA.

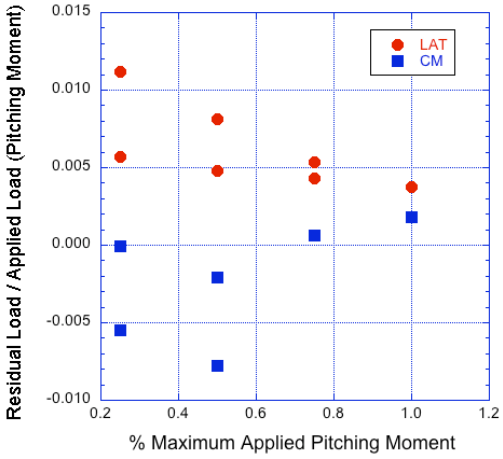

Figure 20. Sample Balance Check Load Results: Loading Applied to CM at ΔX/D = -0.50.

Data runs were performed in Test 24-AA for a jet-off condition as well as for three different values of thrust coefficient (Low, Nominal, and High), with the plenum set pressures varying as a function of freestream Mach number. The plenum temperature was kept at a constant value of 600 °R and plenum pressure was maintained within a certain tolerance of its set value during a run. Because the thrust was non-metric, no wind-off thrust tares were required for the calculation of the jet interactions. For Test 25-AA, only the Low and High thrust coefficient values were run to bracket the effect and to reduce the size of the test matrix to fit within budgetary constraints.

During Test 24-AA, four replicate runs were obtained for each model configuration at the end of that particular block of runs. The replicate runs were randomized over Mach number, sideslip angle, and thrust coefficient in order to characterize data repeatability and uncertainty over the larger parameter space. The same process was used for Test 25-AA, but with three replicate runs.

For each test, two verification pressures were supplied separately to two ports on each ESP module by high-accuracy Mensor (Test 24-AA) or Ruska (Test 25-AA) pressure standards. The differences between the pressure standards and ESP measurements were monitored continuously to check for any drift in the ESP system that would warrant an in-situ calibration of the ESP modules.

The data acquisition system in each facility was configured to acquire data only if certain set-point tolerances were met, as specified in Table 4. The CM and LAT balances were monitored for excessive static/dynamic loads, with audible alarms sounding if limits were exceeded. Additionally, the calculated nozzle discharge coefficient was monitored for values exceeding unity, which would indicate a leak in the high-pressure air system.

Table 4. Specified Set Point Tolerances for Data Acquisition.

Test	M_∞	P_T, psf	T_T, R	$P_{T,J}$, psia	α, deg	β, deg	Specific Humidity, lbm_{H2O} / lbm_{AIR}
24-AA	±0.01	±3	±3	±5	±0.05	±0.10	±0.0003
25-AA	±0.01	±4	N/A	±10	±0.05	±0.05	N/A

Pre-test estimates were made of the buoyancy effects using the cross-sectional area distributions of the models along with calibrated test section static pressure distributions. Results showed that buoyancy corrections would be smaller than the estimated uncertainty on drag measurements and were thus not included in the data reduction. No attempts were made to ascertain flow angle from the measured force data due to the difficulties in obtaining reliable flow angle measurements with low-lift configurations. Likewise, no transonic wall interference corrections were made for Test 24-AA in AEDC 16T. Axial force corrections to the CM were made for the differences between the base pressure and sting-cavity pressure, as applied to the sting-cavity area. Similar corrections were made to the LAT axial force for the metric break pressures.

Shock and jet plume visualization was acquired during Test 24-AA using a method known as Background-Oriented Schlieren (BOS), since the porous test section walls precluded the use of large optical windows needed for traditional schlieren flow visualization. In BOS, a portion of one test section wall was painted with a silver retro-reflective paint, overlaid with a pattern of small black dots. Illumination lamps and a camera are located behind small optical ports in the opposing wall. During a run, density gradients in the flow field cause an apparent shift in the position of the black dots relative to a wind-off image, and specialized software is used to calculate displacement vectors and create images that resemble standard schlieren photographs. An example image from Test 24-AA is shown in Figure 21.[12]

A standard schlieren system was used for Test 25-AA, with images acquired using a high-resolution digital video camera for both single image "stills" and video clips. An example image from Test 25-AA is given in Figure 22.

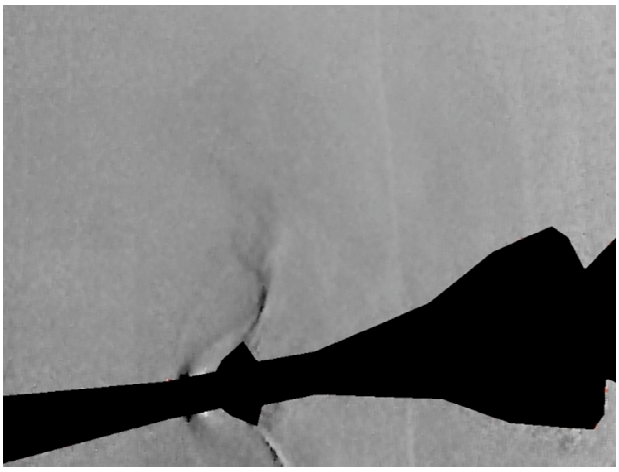

Figure 21. Example BOS Image from Test 24-AA, Mach 1.20, ΔX/D = -0.50.

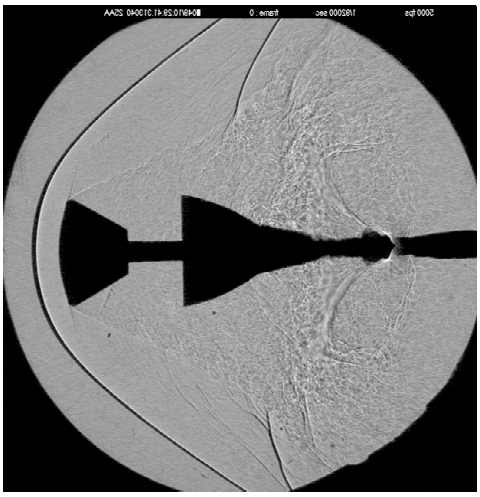

Figure 22. Example Schlieren Image from Test 25-AA, Mach 2.50, ΔX/D = -1.00.

Data were reduced via a combination of standard facility methods and customer-supplied equations and software. The jet stagnation pressure was taken as the average of the three total pressures measured in the model plenum and used, along with the averaged plenum temperature and measured nozzle dimensions, to calculate the ideal mass flow rate and nozzle exit conditions. The NASA LaRC GASPROPS code[13] was used in those calculations to account for real-gas effects resulting from the combination of high plenum pressures and relatively low plenum temperatures. Nozzle thrust was calculated using the venturi-measured mass flow rate in the momentum term of the thrust equation.

Prior to the start of Test 24-AA, the customer team wrote a number of software scripts for rapid processing of the data during the test. Initially, a Perl script was developed to query the Orion aerodynamic database (via the Orion Application Programming Interface (API) tool) and return database aerodynamic coefficients at the exact wind tunnel test conditions, while an additional series of Perl scripts were implemented to compute the JI/proximity increments. This allowed near-real-time plot comparisons of the test data with the existing aerodynamic database using AEDC's DataMine plotting software, and permitted the test team to make rapid changes to the test matrix to address deficiencies in the database. The software effort was coordinated with AEDC in advance and tested using dummy data files supplied by AEDC. The in-situ data processing proved to be a valuable capability, and thus it was replicated in its entirety, including AEDC's DataMine software, for Test 25-AA at NASA Ames.

VII. Results and Discussion

Because of the large volume of data – approximately 2000 air-on runs, 400,000 data points, and 7 independent variables, including 11 different Mach number settings – no more than a sampling of results can be shown here. Data were selected from Test 24-AA at $M_\infty = 0.50$ and from Test 25-AA at $M_\infty = 2.00$ to show some basic effects of axial and vertical separation distance, relative angle of attack, angle of sideslip, and thrust coefficient on both the LAT and CM aerodynamic characteristics. Examples of CM surface pressure coefficient data from Test 24-AA are presented, and results from both tests are given to illustrate aerodynamic coefficient repeatability. Due to export control restrictions on the data, plots are shown with no scales on the y-axes.

The effect of axial separation distance on the longitudinal aerodynamic coefficients at $M_\infty = 0.50$ is shown in Figure 23 for a nominal thrust coefficient setting and a sideslip angle, $\beta = 0°$. Of particular interest is the effect on axial force coefficient, C_A, for both the CM and LAT. In a ±5-degree angle of attack range around 180°, the flow between the two bodies and in the wake of the CM sets up a strong suction force that results in a large increase in axial force on the CM and a concomitant reduction in axial force for the LAT, particularly at the intermediate axial separation distances. (Note that because of the coordinate axis definition for the vehicle, the axial force coefficient is negative, with increasing magnitude towards the bottom of the plot.) As $\Delta X/D$ increases towards one body diameter, the suction force and thus C_A lessens for the CM, but remains at about the same level for the LAT as the interior of the BPC cavity sees more of a ram air effect. The axial separation distance has a larger effect on pitching moment for the LAT than for the CM, with sharp changes in longitudinal stability around $\alpha = 180°$.

The corresponding effect of axial separation distance for supersonic conditions is shown in Figure 24 for a freestream Mach number, $M_\infty = 2.00$. Here, the axial force coefficient for the CM shows a general monotonic increase in magnitude with increasing $\Delta X/D$, and the local maxima shift towards $\alpha = 165°$. The trends in C_N and C_m show a sharp change in character between $\Delta X/D = -0.25$ and -0.50 and for angles of attack, $\alpha < 162°$. For the LAT, C_A is relatively flat for $\alpha > 165°$, with strongly increasing C_A at lesser angles for the larger axial separation distances as the BPC cavity is no longer shielded by the CM and sees more direct flow impingement.

The effect of sideslip on the lateral-directional aerodynamic characteristics at $M_\infty = 2.00$ is illustrated in Figure 25. In general, some lack of symmetry exists in the positive and negative sideslip data taken about the zero-sideslip condition – a trend that was seen throughout both tests. This is due in part to the asymmetric geometry on the inside of the BPC cavity. Because of the relatively smooth, axisymmetric OML, the measured rolling moments were small and more or less within the balance calibration uncertainty, particularly for the CM.

Thrust coefficient effects are highlighted in Figure 26 for $M_\infty = 0.50$ and $\beta = 0°$. The jet-off condition exhibits an almost discontinuous increase in CM axial force coefficient spanning a 10-degree angle of attack range centered near, but not exactly at, $\alpha = 180°$, and the LAT shows a related decrease in C_A. With the JM nozzles blowing, the axial force coefficient decreases with increasing C_F, and the drag "bucket" is less abrupt but now centered at $\alpha = 180°$. For the CM, normal force and pitching moment show changes from a jet-off to a jet-on condition, but virtually no differences amongst the three jet-on conditions tested. The LAT is influenced more strongly by the particular thrust coefficient setting, likely due to the closer proximity of the LAT to the JM plumes. Normal force shows a strong change from the jet-off condition, and subsequent increases at greater values of C_F. Longitudinal stability is likewise primarily influenced by the presence of the JM plumes and less by the particular thrust coefficient setting. This general trend – large changes from jet-off to jet-on, and smaller changes due to C_F – was observed throughout the two tests. An interesting feature noted in Figure 26 is the periodic oscillation in C_N on the LAT in a narrow region around $\alpha = 180°$ for the jet-off condition, and caused by unsteady flow and consequent model dynamics.

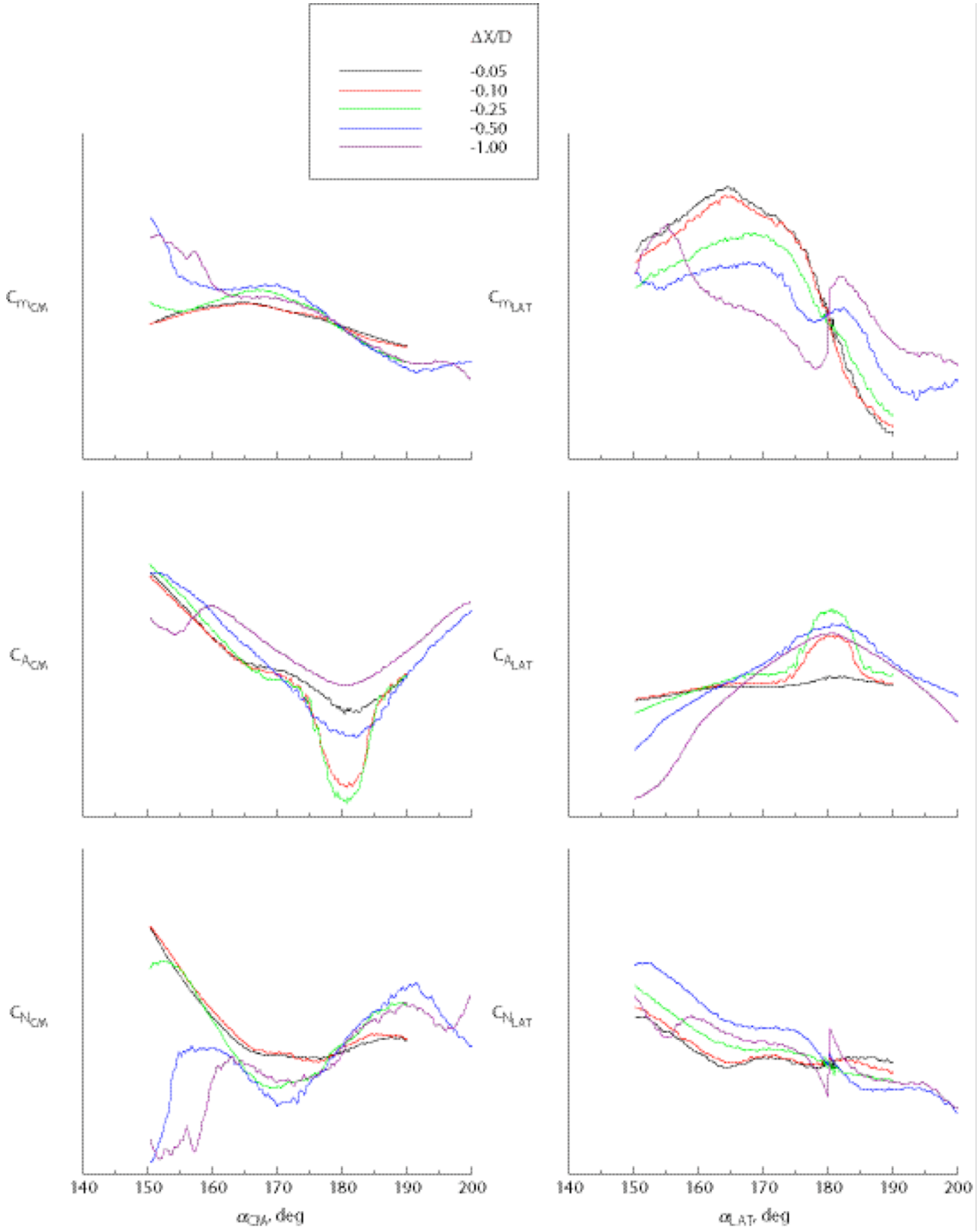

Figure 23. Effect of ΔX/D at M_∞ = 0.50, β = 0°, ΔZ/D = 0, Δα = 0°, C_F = Nominal.

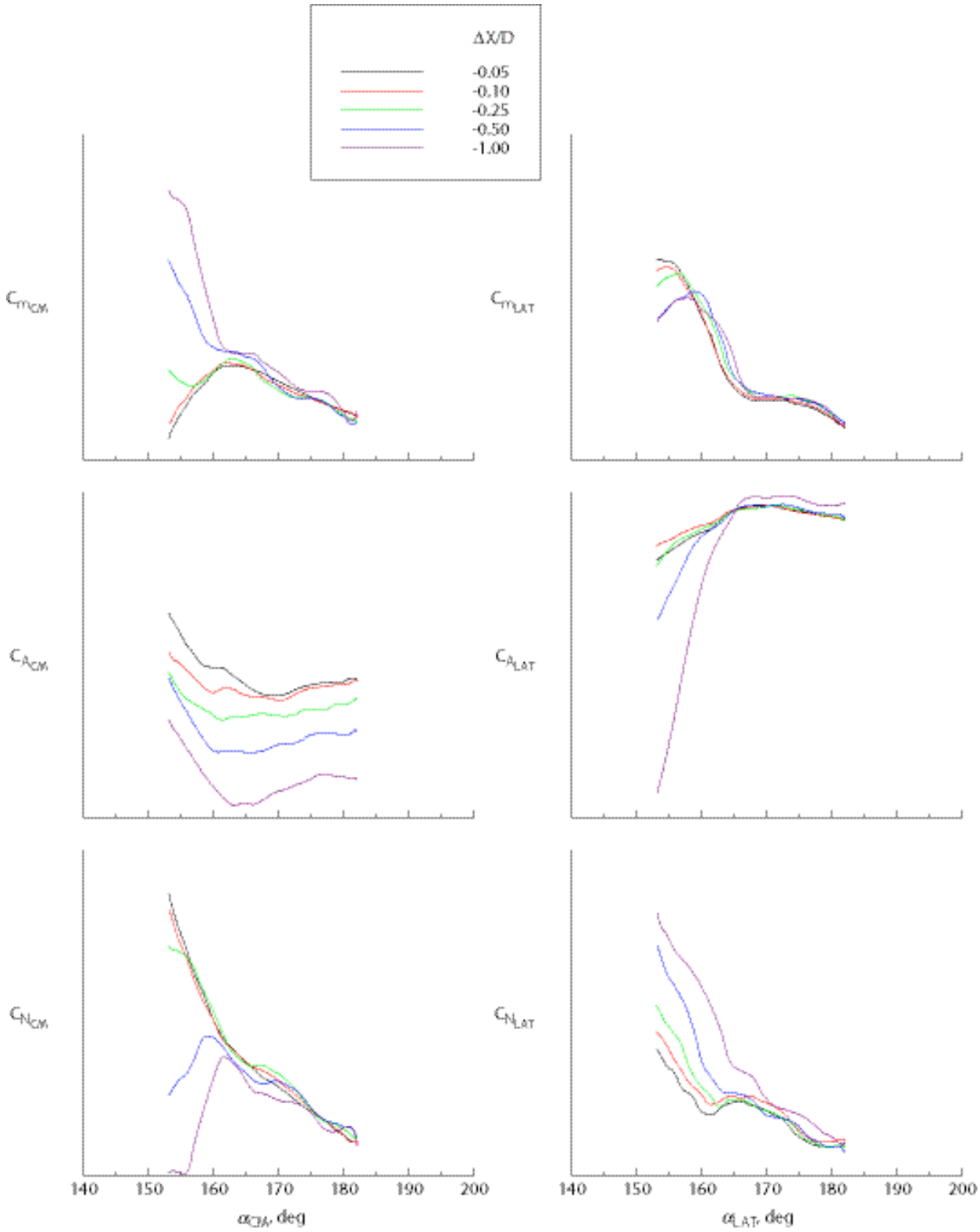

Figure 24. Effect of ΔX/D at M_∞ = 2.00, β = 0°, ΔZ/D = 0, Δα = 0°, C_F = Nominal.

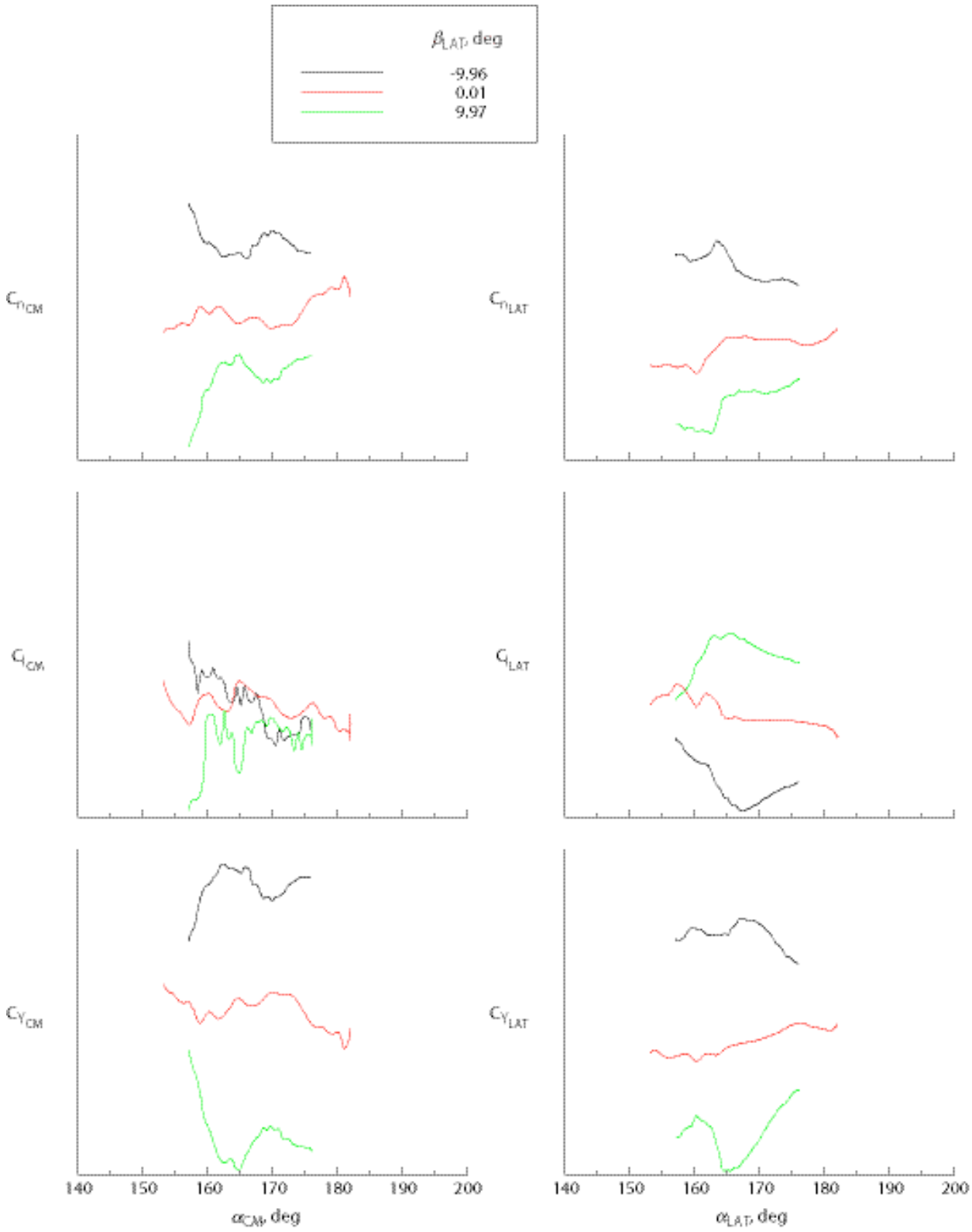

Figure 25. Effect of β at M_∞ = 2.00, ΔX/D = -0.50, ΔZ/D = 0, Δα = 0°, C_F = Nominal.

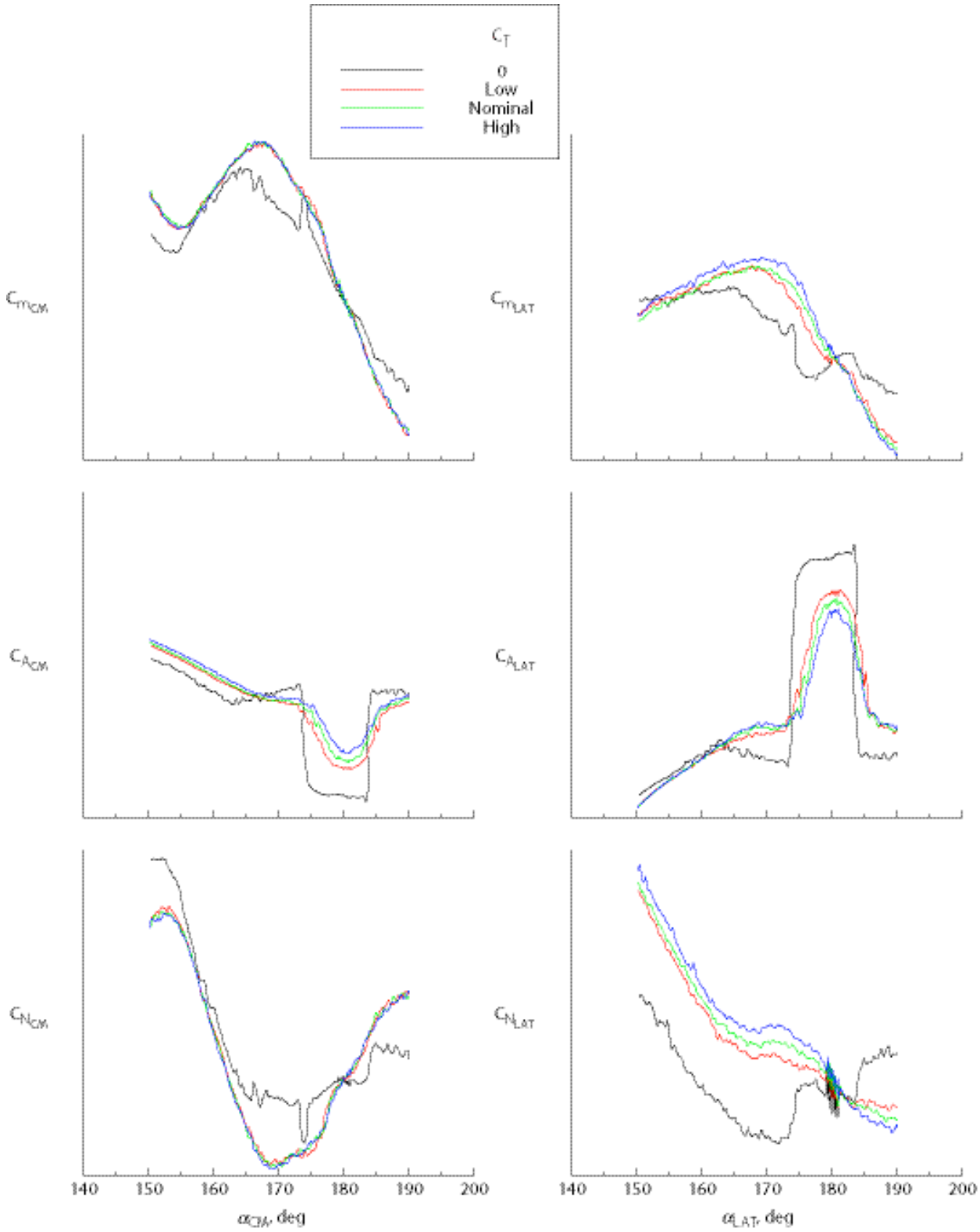

Figure 26. Effect of C_F at $M_\infty = 0.50$, $\beta = 0°$, $\Delta X/D = -0.25$, $\Delta Z/D = 0$, $\Delta\alpha = 0°$.

The effects of ΔZ/D and Δα on the CM pitching moment coefficient are presented in Figure 27 for M_∞ = 0.50, β = 0°, ΔX/D = -1.00, and both jet-off and jet-on (nominal C_F) conditions. Here, the curves are shown as "deltas" (DCMCMS) from CM-only configuration (always a jet-off condition), and are the result of the post-test processing of the data that also produced information at intermediate values of ΔZ/D and Δα not run in Test 24-AA. In this example, the effects of ΔZ/D and Δα are relatively small, with minimum influence of the JM plumes at the maximum axial separation distance. The delta-coefficients were computed from the entire set of data for both the CM and LAT relative to the respective CM-only and LAT-only configurations, and used in the construction of the Orion aerodynamic database.[14]

Examples of data repeatability for Test 24-AA and Test 25-AA are given in Figure 28 and Figure 29, respectively. The former is for the closest separation distance of ΔX/D = -0.02 while the latter is for ΔX/D = -0.50; both cases are for β = 0° and a nominal thrust coefficient setting. As shown in Figure 28, the data are repeatable between the two runs, with the exception of C_A for both the CM and LAT. Axial force coefficient proved to have the largest uncertainty in the longitudinal aerodynamic coefficients for Test 24-AA. Figure 29 illustrates the generally better data repeatability for Test 25-AA. As discussed earlier, replicate runs were randomized over a subset of the parameter space and performed as a block at the end of each model configuration. Facility occupancy time and budget limitations did not permit the re-testing of an earlier model configuration that would have yielded an assessment of longer-term data repeatability, including installation and model geometry effects associated with the rebuild of a model configuration. Data uncertainties were quantified as part of the aerodynamic database development process and are summarized in Table 5 for the CM and Table 6 for the LAT.

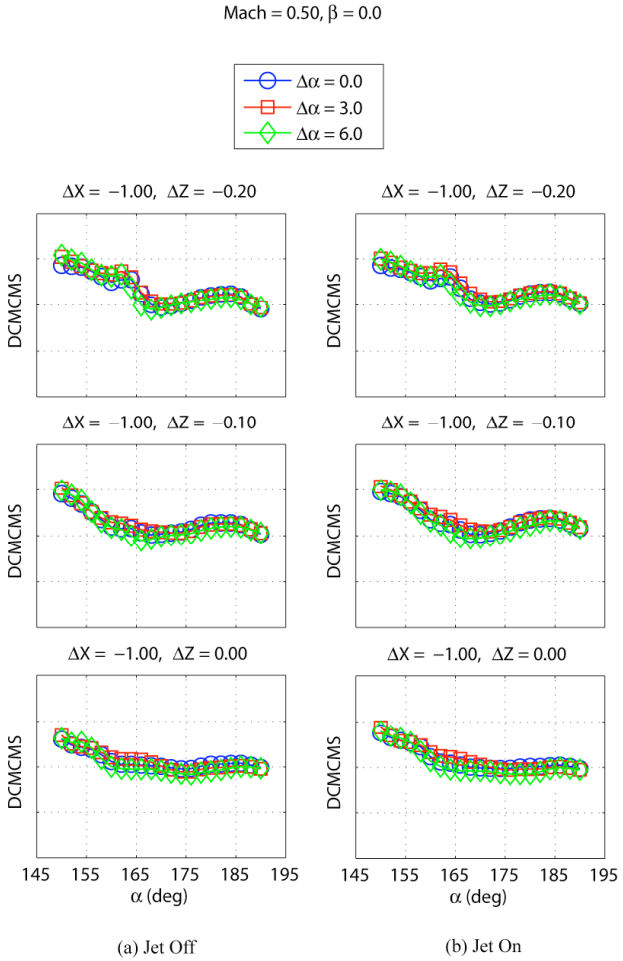

Figure 27. Effect of ΔZ/D and Δα at M_∞ = 0.50, β = 0°, ΔX/D = -1.00, C_F = 0 and Nominal.

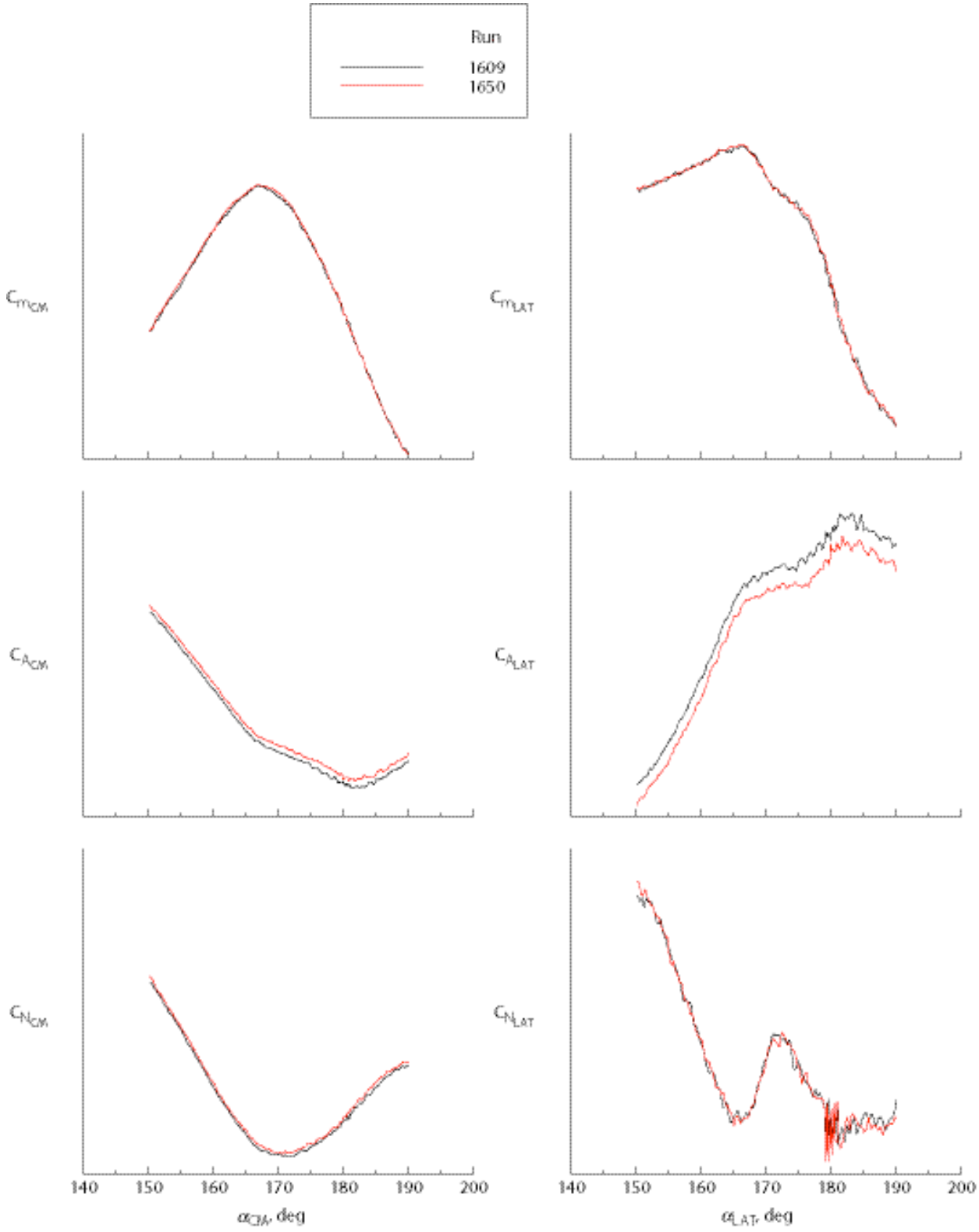

Figure 28. Repeatability at $M_\infty = 0.50$, $\beta = 0°$, $\Delta X/D = -0.02$, $\Delta Z/D = 0$, $\Delta\alpha = 0°$, C_F = Nominal.

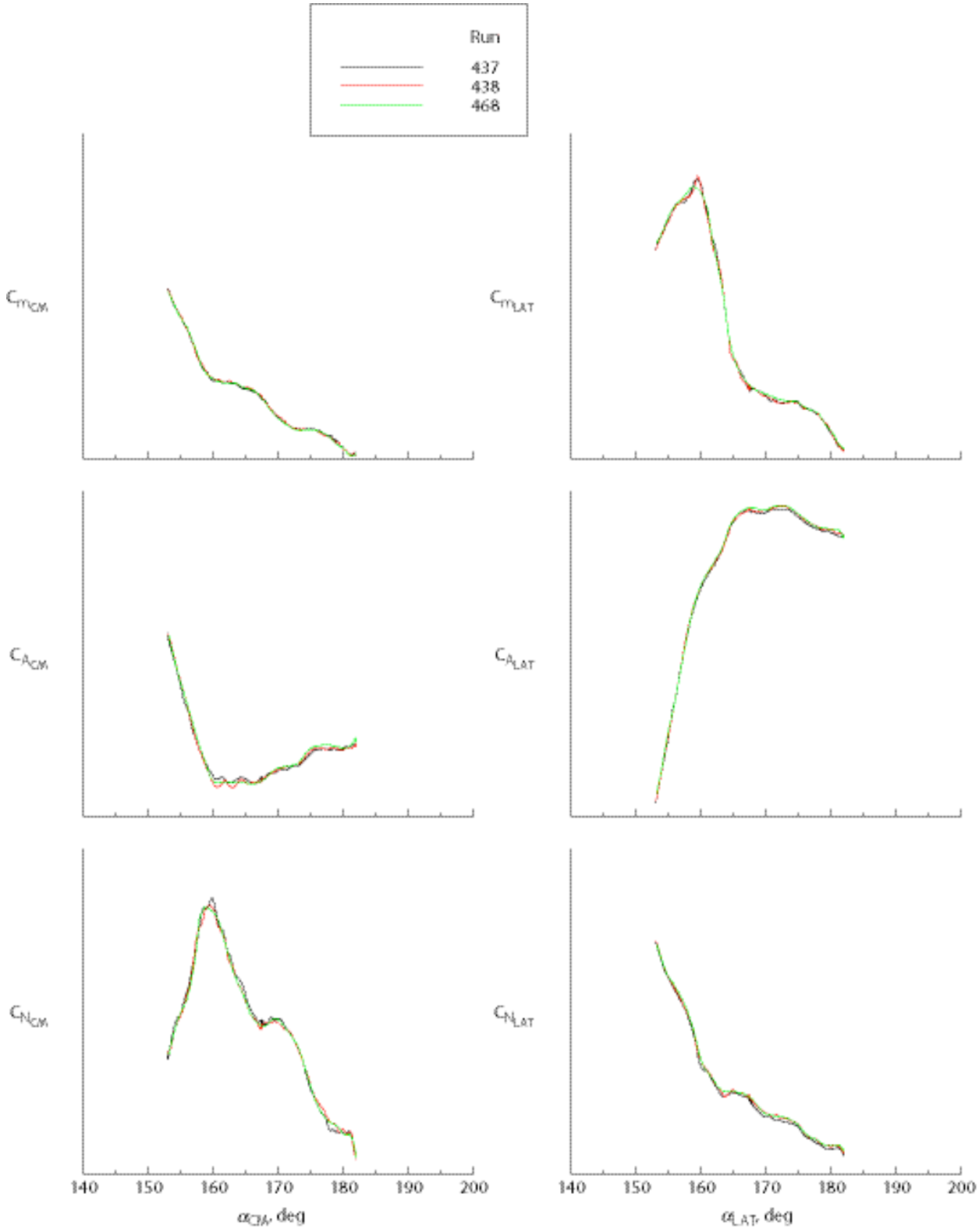

Figure 29. Repeatability $M_\infty = 2.00$, $\beta = 0°$, $\Delta X/D = -0.50$, $\Delta Z/D = 0$, $\Delta\alpha = 0°$, C_F = High.

Table 5. Test 24-AA / 25-AA Data Uncertainties for the Crew Module (CM).

Test	M_∞	UC_A	UC_Y	UC_N	UC_l	UC_m	UC_n
24-AA	0.3	0.0064	0.0059	0.0049	0.00015	0.0042	0.0047
	0.5	0.0064	0.0024	0.0031	0.00011	0.0020	0.0020
	0.7	0.0077	0.0021	0.0044	0.00018	0.0030	0.0021
	0.9	0.0043	0.0015	0.0044	0.00009	0.0030	0.0012
	1.1	0.0044	0.0011	0.0011	0.00006	0.0011	0.0011
	1.2	0.0038	0.0012	0.0016	0.00004	0.0012	0.0010
25-AA	1.6	0.0024	0.0016	0.0009	0.00014	0.0007	0.0011
	1.8	0.0019	0.0010	0.0005	0.00007	0.0003	0.0007
	2.0	0.0026	0.0022	0.0009	0.00019	0.0007	0.0016
	2.2	0.0023	0.0011	0.0005	0.00007	0.0004	0.0008
	2.5	0.0011	0.0013	0.0007	0.00015	0.0006	0.0009

Table 6. Test 24-AA / 25-AA Data Uncertainties for the Launch Abort Tower (LAT).

Test	M_∞	UC_A	UC_Y	UC_N	UC_l	UC_m	UC_n
24-AA	0.3	0.0146	0.0186	0.0111	0.00041	0.0049	0.0095
	0.5	0.0114	0.0138	0.0141	0.00031	0.0073	0.0058
	0.7	0.0106	0.0197	0.0178	0.00065	0.0075	0.0111
	0.9	0.0088	0.0215	0.0121	0.00021	0.0070	0.0130
	1.1	0.0075	0.0202	0.0108	0.00041	0.0064	0.0107
	1.2	0.0043	0.0048	0.0050	0.00023	0.0070	0.0061
25-AA	1.6	0.0069	0.0068	0.0057	0.00137	0.0063	0.0038
	1.8	0.0070	0.0062	0.0076	0.00150	0.0086	0.0062
	2.0	0.0088	0.0082	0.0066	0.00185	0.0077	0.0064
	2.2	0.0076	0.0087	0.0049	0.00040	0.0052	0.0055
	2.5	0.0044	0.0069	0.0037	0.00087	0.0044	0.0056

VIII. Summary

Two wind tunnel tests were performed at transonic and supersonic speeds to determine the combined aerodynamic effects of proximity and jet interaction on the CM and LAT during post-abort LAT jettison. Approximately 400,000 data points were acquired in 2000 runs covering a parameter space of seven independent variables, including relative separation movements between the CM and LAT, thrust settings for the JM nozzles, Mach number, and vehicle attitude. The ranges of the independent variables were established from Monte Carlo trajectory simulations using pre-test estimates of the aerodynamic characteristics along with various trajectory and mass properties models. The JM nozzle geometries for the wind tunnel model were determined from fluids-based scaling equations along with flight rocket motor performance data, while predictions were made of the JM nozzle plume shape to ensure that the wind tunnel model plumes were representative of the flight case. Body-axis

aerodynamic data were obtained for the CM and LAT from force balance instrumentation and used in the development of the Orion aerodynamic database, while surface pressure data were obtained for structural loads estimation as well as to serve as benchmark for CFD predictions.

Acknowledgments

The authors would like to thank the staff of the Arnold Engineering Development Center and NASA Ames Research Center for their efforts in making these tests a success. In particular, we would like to thank Mr. Charlie Smith (retired) of Aerospace Testing Alliance, AEDC and Mr. Chris Natividad (retired) of the NASA Ames Research Center, who served as the principal test engineers at their respective facilities. Additional thanks go to the Orion team members who supported the wind tunnel tests in various capacities: Karen Bibb, Greg Brauckmann, Bruce Owens, and Eric Walker of the NASA Langley Research Center; Aliyah Ali, Jim Greathouse, Phil Robinson, Paul Romere (retired), and Alan Schwing of the NASA Johnson Space Center; Jim Ross of the NASA Ames Research Center; and Jared Cross and David Mayfield of Lockheed Martin Space Systems, Denver, CO.

References

1. "NASA's Exploration Systems Architecture Study – Final Report," NASA TM-214062, 2005.
2. Smith, C.L. and Reinholtz, C.K., "Documentation of a Wind Tunnel Test to Investigate the Separation Characteristics of the Orion Launch Abort Vehicle During Launch Abort Tower Jettison," AEDC-TR-09-F-31, October 2009.
3. Pindzola, M., "Jet Simulation in Ground Test Facilities," AGARDograph 79, November 1963.
4. Lilley, J.S. and Hoffman, J.D., "Performance Analysis of Scarfed Nozzles," *Journal of Spacecraft and Rockets*, Vol. 23, No. 1, 1986.
5. Salas, M.D., "The Numerical Calculation of Inviscid Plume Flow Fields," AIAA Paper 1974-523, June 1974.
6. CAP Aerodynamics Team, "Orion Aerodynamic Databook, Version 0.54.1," NASA CXP-72167, November 2009.
7. Daum, F.L. and Gyarmathy, G., "Condensation of Air and Nitrogen in Hypersonic Wind Tunnels," *AIAA Journal*, Vol. 6, No. 3, 1968.
8. *AEDC Test Facilities Handbook, 13th Edition*, Arnold Engineering Development Center, Arnold AFB, TN, May 1992.
9. "Test Planning Guide for High Speed Wind Tunnels, Rev 5," http://www.windtunnels.arc.nasa.gov
10. Smith, R.E. and Matz, R.J., "Verification of a Theoretical Method for Determining Discharge Coefficients for Venturis Operating at Critical Flow Conditions," AEDC-TR-61-8, September 1961.
11. Braslow, A.L., Hicks, R.M., and Harris, R.V., Jr., "Use of Grit-Type Boundary-Layer-Transition Strips on Wind-Tunnel Models," NASA TN-D-3579, 1966.
12. Reinholtz, C.K., Heltsley, F.L., Scott, K.E., and Rhode, M.N., "Visualization of Jettison Motor Plumes from an Orion Launch Abort Vehicle Wind Tunnel Model Using Background-Oriented Schlieren," AIAA Paper 2010-1736, February 2010.
13. Hollis, B.R., "Real-Gas Flow Properties for NASA Langley Research Center Aerothermodynamic Facilities Complex Wind Tunnels," NASA CR-4755, 1996.
14. Chan, D., Walker, E., Robinson, P., Wilson, T., and Shestopolov, A., "Modeling Powered Aerodynamics for the Orion Launch Abort Vehicle Aerodynamic Database, 29th AIAA Applied Aerodynamics Conference, Honolulu, HI, June 2011 (submitted for publication).